A distinctive rare earth element signature for pyrite oxidation and glacial weathering

Kwangchul Jang, Germain Bayon, Olivier Pourret, Young Jin Joe, Jung-Hyun Kim, Eunji Byun, Matthias Forwick, Rafael León, Seung-Il Nam

A distinctive rare earth element signature for pyrite oxidation and glacial weathering

Kwangchul Jang[a,b], Germain Bayon[c], Olivier Pourret[d], Young Jin Joe[a], Jung-Hyun Kim[a], Eunji Byun[b], Matthias Forwick[e], Rafael León[f], and Seung-Il Nam[a,*]

[a]Division of Glacier and Earth Sciences, Korea Polar Research Institute; 21990 Incheon, Republic of Korea.

[b]Department of Earth System Sciences, Yonsei University; 03722 Seoul, Republic of Korea.

[c]Univ Brest, CNRS, Ifremer, Geo-Ocean, F-29280 Plouzané, France.

[d]AGHYLE, UniLaSalle, Beauvais, France.

[e]Department of Geosciences, UiT The Arctic University of Norway; NO-9037 Tromsø, Norway.

[f]Department of Earth Sciences and Research Center on Natural Resources, Health and the Environment, University of Huelva, E-21071 Huelva, Spain.

Submitted to *Chemical Geology*, October 2023

1st Re-submitted to *Chemical Geology*, March 2024

2nd Re-submitted to *Chemical Geology*, May 2024

*Corresponding author. E-mail: sinam@kopri.re.kr, ORCID : 0000-0003-0006-0153

Abstract

The application of rare earth elements (REE) and neodymium (Nd) isotopes to authigenic Fe-(oxyhydr)oxide phases leached from marine sediments can be used for reconstructing past ocean circulation and chemical weathering patterns on nearby continental landmasses. To explore the behaviour of REE during chemical weathering in glacial environments, we analyzed the authigenic fraction of glacimarine sediments from the continental shelf off northern Svalbard (Arctic Ocean), where the evolution of ice sheet dynamics since the last deglaciation is well constrained. Our results show that leached authigenic fractions in Svalbard sediments exhibit shale-normalized REE patterns characterized by anomalously high mid-REE enrichment relative to both light- and heavy-REE, as expressed by concavity index values (CI > 2.5) that significantly depart from typical REE signatures for leached fractions in marine and river sediments worldwide. Using a compilation of literature data, we provide compelling evidence that the occurrence of pronounced mid-REE enrichment in authigenic fractions of Svalbard marine sediments links to terrestrial oxidation of pyrite following glacial weathering. While future investigation will be required to further understand the detailed mechanism accounting for the observed REE decoupling and its link to pyrite oxidation, we propose that preferential dissolution of MREE-enriched rock-bearing minerals such as apatite following glacial erosion, sulfide weathering and subsequent release of sulfuric acid could release a distinctive REE signature in glacial surface environments. Our findings suggest that the use of authigenic REE in the sedimentary record could provide a means for tracing glacial weathering and associated biogeochemical sulfur and iron cycling across geological times.

Keywords: rare earth elements; iron oxyhydroxides; sulfide weathering; sulfur cycle; Arctic coastal environments; glacier retreat;

1. Introduction

In recent decades, the rare earth elements (REE) and their isotope ratios have been increasingly used as paleoenvironmental tracers in authigenic phases extracted from marine sediments (e.g., Dias et al., 2021; Frank, 2002; Jang et al., 2017; Larkin et al., 2022). The rationale behind the use of REE in sedimentary Fe-(oxyhydr)oxide phases as paleoceanographic archives is that they incorporate - upon formation near the sediment-seawater interface – the neodymium (Nd) isotopic composition ($^{143}Nd/^{144}Nd$) of ambient bottom-water masses. Measurements of Nd isotope ratios in leached fractions of marine sediments from open ocean settings have thus been used to reconstruct, for instance, the evolution of deep-ocean circulation over glacial-interglacial timescales (e.g., Böhm et al., 2015; Piotrowski et al., 2004; Roberts et al., 2010; Rutberg et al., 2000). At ocean margins, the leached Fe-(oxyhydr)oxide component of marine sediments can be strongly influenced by terrestrial inputs, due to the presence of continentally-derived Fe-(oxyhydr)oxides transported along with the fine-grained terrigenous material delivered to the seafloor (e.g., Bayon et al., 2004; Jang et al., 2020, 2021; Kraft et al., 2013; Werner et al., 2014). Such continentally-derived Fe-(oxyhydr)oxides can include secondary weathering products formed in soils, Fe-(oxyhydr)oxide phases derived from the erosion of ancient sedimentary rock formations in source regions, or iron oxides precipitated from Fe-rich glacial meltwater upon mixing with seawater.

Recent studies conducted on lake (Süfke et al., 2019) and river sediments worldwide (Bayon et al., 2020) have both highlighted the great potential of using REE and Nd isotopes in sedimentary iron oxides for tracing chemical weathering in corresponding watersheds. Recently, Bayon et al. (2020) introduced a novel index termed ‘concavity index’ (CI) as a quantitative measure of mid-REE (MREE) enrichments relative to light- and heavy-REE that can be used for discerning the provenance of leached Fe-(oxyhydr)oxide components in sediments. One striking finding of this study was the fact that a few leached sediments from catchments draining extensive shale formations, such as the Mackenzie (Canada) and Gaoping (Taiwan) rivers, displayed anomalously high MREE enrichments, yielding CI values much higher than the general range of values typically encountered for oxide fractions in both marine and river sediments. Because these particular watersheds had been previously

shown to be the location of intense sulfide weathering, such anomalously high MREE signatures in leached river sediments were hypothetically attributed to the presence of secondary Fe-(oxyhydr)oxides resulting from terrestrial pyrite oxidation in shale formations (Bayon et al., 2020).

Building on these recent findings, we have investigated the REE distribution in oxide fractions leached from glacimarine sediments (site HH17-1085-GC) on the continental shelf off northern Svalbard in the Arctic Ocean (Fig. 1). Because intense pyrite oxidation is thought to dominate in glacial environments (Anderson et al., 2000; Calmels et al., 2007; Stachnik et al., 2022; Torres et al., 2017), our main goal was to further explore the hypothesis that REE in sedimentary Fe-(oxyhydr)oxide phases can be used to trace oxidative sulfide weathering. This research has broad implications given the presumed importance of oxidative weathering in the global evolution of atmospheric oxygen and carbon levels in Earth's history (Konhauser et al., 2011; Liu et al., 2023; Torres et al., 2017; Ostrander et al., 2021).

2. Study Area

Sediment core HH17-1085-GC (hereafter 1085; 80.274ºN, 16.211ºE, 462 cm long) was retrieved from 322 m water depth on the continental shelf offshore northern Svalbard during a Korean-Norwegian joint cruise on *RV Helmer Hanssen* in 2017 (Jang et al., 2021) (Fig. 1). The Svalbard archipelago, at the border of the Arctic Ocean is composed of nine main islands including Spitsbergen, Nordaustlandet, Barentsøya and Edgeøya (Fig. 1). The bedrock geology in Svalbard includes various sedimentary, metamorphic and igneous rock formations with ages ranging from late Archaean to Cenozoic (Dallmann and Elvevold, 2015). Among them, the Devonian Old Red sandstone outcropping west of Wijdefjorden represents the main source rock for sediments deposited at Site 1085, together with Proterozoic metamorphic rocks east of Wijdefjorden, and Neoproterozoic and Permian to Carboniferous rocks on Nordaustlandet (Jang et al., 2021).

Svalbard has experienced major ice sheet fluctuations during the late Quaternary. During the last glacial maximum, the Svalbard-Barents Sea Ice Sheet covered the inner continental shelf offshore northern and western Svalbard (Hughes et al., 2016 and references therein), including the location of

Site 1085 (Jang et al., 2021). After 16.3 ka, gradual ice sheet retreat occurred, punctuated by short-term glacier halts and/or re-advances, until reaching a minimum glacier extent in Svalbard during the middle Holocene (Allaart et al., 2020; Farnsworth et al., 2020; Jang et al., 2021). The late Holocene period witnessed a phase with re-advances of terrestrial and tidewater glaciers in Svalbard (Forwick and Vorren, 2009; Jang et al., 2021; Røthe et al., 2015; Svendsen and Mangerud, 1997).

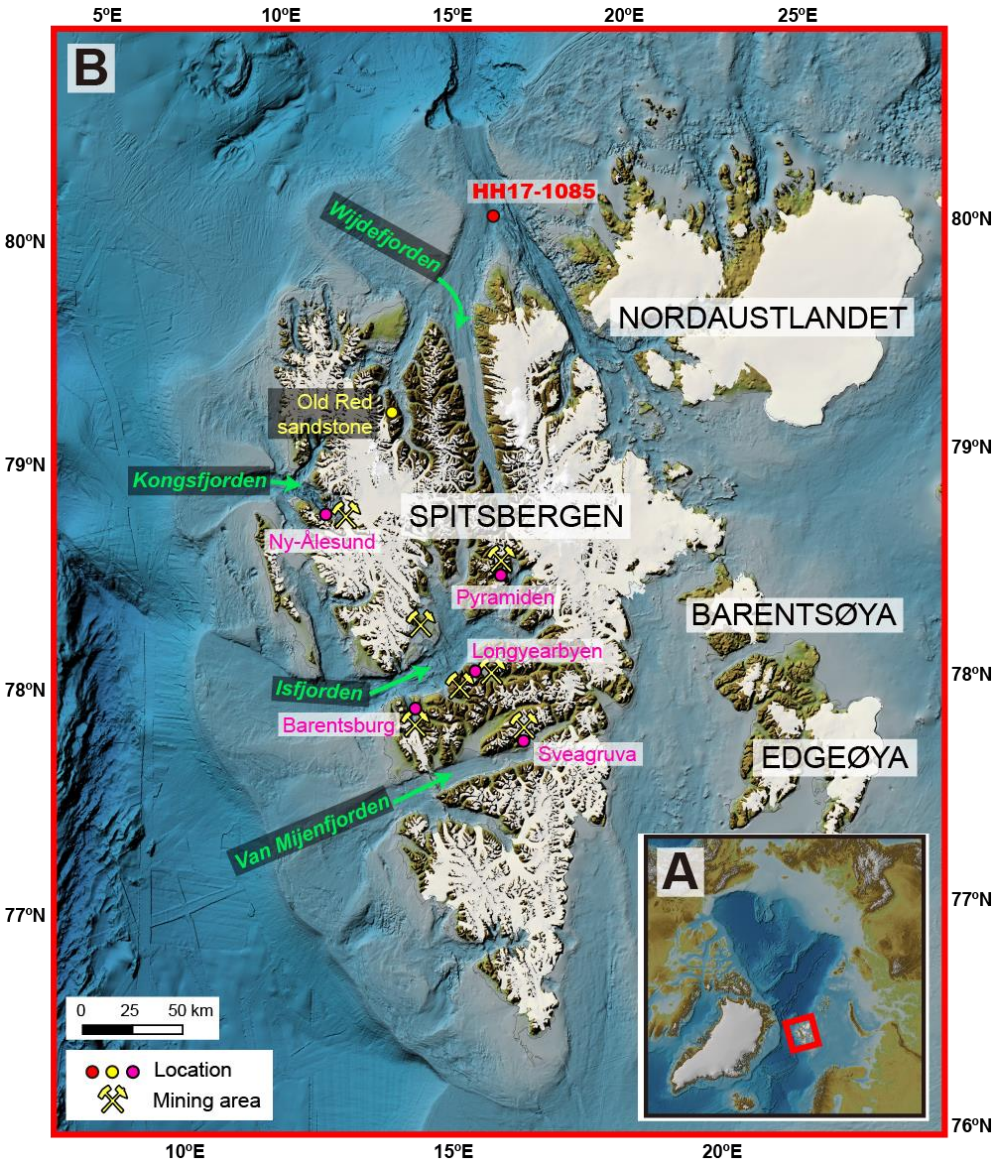

Fig. 1. Map of (A) the Arctic Ocean and (B) Svalbard. Sampling locations for core HH17-1085-GC and the Devonian Old Red sandstone are indicated with yellow and red circles, respectively. Locations for coal mining activity are also marked with yellow cross symbols. The bathymetric information is based on IBCAO 4.0 bathymetric grid (Jakobsson et al., 2020) combined with the published seafloor information (Allaart et al., 2020). Note that all mines, except for those in Longyearbyen and Barentsburg, are no longer in operation.

3. Materials and Methods

3.1. Sample collection

The sediment core HH17-1085-GC, retrieved from the continental shelf offshore northern Svalbard, was subsampled at 5-25 cm intervals (n = 29). Subsequently, the subsamples were freeze-dried and homogenously powdered for geochemical analyses. For comparison, a representative sample of the Devonian Old Red sandstone was collected from the Wood Bay formation in Halvdanpiggen, Woodfjorden (ID 080302; 79.389ºN, 13.622ºE; Jang et al., 2020) (Fig. 1). This bedrock sample was also powdered homogenously.

Core 1085 displays four distinctive sedimentary facies (Jang et al., 2021): laminated mud (between 462-385 cm sediment depth), weakly laminated mud (385-228 cm), massive mud (228-30 cm) and bioturbated sandy mud (30-0 cm) (Fig. 2). A coarse-grained layer is discernible at a depth of 360-370 cm within the weakly laminated mud facies. According to the age model based on radiocarbon dating (Jang et al., 2021), the sediment interval exhibiting laminated structures (462-228 cm) broadly covers the last deglaciation during the late Pleistocene (16.3 to 12.1 ka), while the massive mud and bioturbated were predominantly deposited during the early-to-middle (12.1 to 2.7 ka) and late Holocene (2.7 ka to modern) periods, respectively (Fig. 2). Sedimentation rates were relatively high until the early Holocene (up to 88 cm/ka) and significantly reduced during the middle Holocene (Jang et al., 2021) (Fig. 2). The sediment starvation or a hiatus during the middle Holocene has also been observed in other Svalbard fjords, likely due to limited or minimum glacigenic input when glaciers in Svalbard reached their Holocene minimum (e.g., Allaart et al., 2020; Farnsworth et al., 2020; Flink et al., 2017; Joe et al., 2022).

3.2. REE and Nd isotope analyses

The REE abundances in leached fractions of core 1085 sediments and the Devonian Old Red sandstone were determined with an Agilent 7900 inductively coupled plasma mass spectrometry (ICP-MS) at the National Instrumentation Center for Environmental Management at Seoul National University (Republic of Korea), following a sequential extraction procedure. Leached fractions were

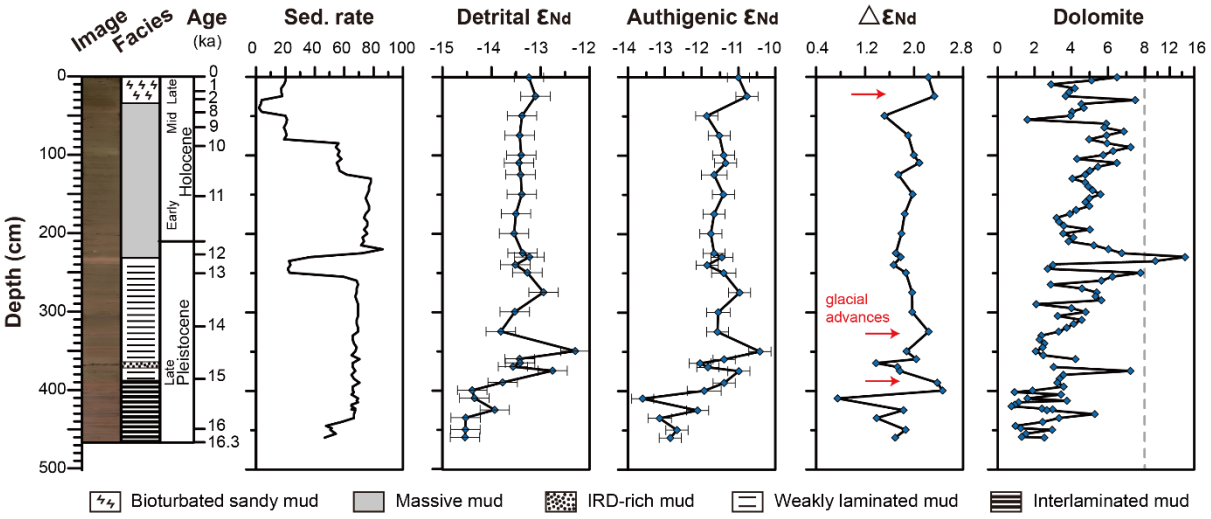

Fig. 2. Summary of lithological and geochemical features at Site 1085. Sedimentation rate (cm/ka), detrital and authigenic ε_{Nd} values, as well as their difference ($\triangle\varepsilon_{Nd} = \varepsilon_{Nd\ Auth} - \varepsilon_{Nd\ Det}$), and dolomite contents are included for comparison. All dataset are sourced from Jang et al. (2021).

136 extracted using 0.02 M hydroxylamine hydrochloride in 25% acetic acid (volume to volume) for 1
137 hour (Jang et al., 2021). This mild leaching protocol was designed to selectively target easily
138 reducible Fe-(oxyhydr)oxides like ferrihydrite and lepidocrocite (Poulton and Canfield, 2005), while
139 minimizing the extraction of undesired reactive phases, including volcanic components (Jang et al.,
140 2017; Wilson et al., 2013). The leachates were evaporated to dryness and taken up in ultrapure diluted
141 HNO_3 solution for ICP–MS analyses. The analytical uncertainty in the REE measurements was ≤ 5%
142 (1 SD). Natural water certified reference materials SLRS-6 and SPS-SW1 were measured to evaluate
143 the accuracy of measured abundances, agreeing well (< 5%) with literature values (Yeghicheyan et al.,
144 2019), except for lutetium (Lu; not used in this study). For comparison purposes, the REE abundances
145 were normalized to the World River Average Silt (WRAS: Bayon et al., 2015), marked with the
146 subscript "N". The degree of MREE enrichment in shale-normalized REE patterns can be quantified
147 numerically by the mean of a 'concavity index' (CI) = $Gd_N/(La^6_N \times Yb^7_N)^{1/13}$ calculated by geometric
148 extrapolation (i.e., semi-logarithmically; Lawrence et al., 2006), following the approach described by
149 Bayon et al. (2020). Using the above equation, the following relationship $(La/Gd)_N = [(Gd/Yb)_N \times$
150 $1/CI]^{7/6}/CI$ can be used to illustrate graphically theoretical CI values in a plot of $(Gd/Yb)_N$ versus
151 $(La/Gd)_N$.

Methods for sample preparation and acquisition of Nd isotopes for both leached and detrital fractions in core 1085 have already been published by Jang et al. (2021). In summary, the same mild leaching protocol described above was used for Nd isotope analyses of authigenic fractions. Conversely, the detrital fraction, which corresponds to the residual material left behind after the extraction of non-silicate fractions from the sediment, was digested by alkaline fusion (Bayon et al., 2009). Neodymium was purified by ion chromatography using the TRU and Ln resins (modified after Pin and Zalduegui, 1997). Subsequently, $^{143}Nd/^{144}Nd$ ratios were measured by thermal ionization mass spectrometry (Triton, Thermo Scientific) at the Korea Polar Research Institute using $^{144}Nd/^{146}Nd$ = 0.7219 for correcting instrumental mass bias. The measured Nd isotope ratios were finally expressed as ε_{Nd}, which is calculated using the following equation:

$$\varepsilon_{Nd} = [(^{143}Nd/^{144}Nd)_{sample}/(^{143}Nd/^{144}Nd)_{CHUR}-1] \times 10^4$$

where $(^{143}Nd/^{144}Nd)_{CHUR}$ is 0.512638 (Jacobsen and Wasserburg, 1980). The $\triangle\varepsilon_{Nd}$ value, a proxy for tracing glacial fluctuations (Jang et al., 2020), is defined as the difference between the leached ε_{Nd} and the detrital ε_{Nd} values.

4. Results and background Nd isotope data

4.1. REE concentrations

The REE abundances in the leached fractions of the Devonian Old Red sandstone and Site 1085 marine sediments are reported as concentrations (μg/g) relative to the initial mass of leached bedrock and bulk sediment (Table 1). The REE concentrations determined for the leached fraction of the Devonian Old Red sandstone are comparatively higher than the leached fraction of sediments at Site 1085 (Fig. 3). For example, the lanthanum (La) and gadolinium (Gd) concentrations of leached fractions for the Devonian Old Red sandstone are 2.6 and 1.0 μg/g, respectively, while those for Site 1085 sediments range from 0.58 to 2.0 μg/g (average ~ 1.2±0.38, 1 SD, n= 29) and 0.30 to 0.79 μg/g (0.56±0.16, 1 SD, n= 29), respectively. Similarly, the ytterbium (Yb) abundance (0.43 μg/g) in the

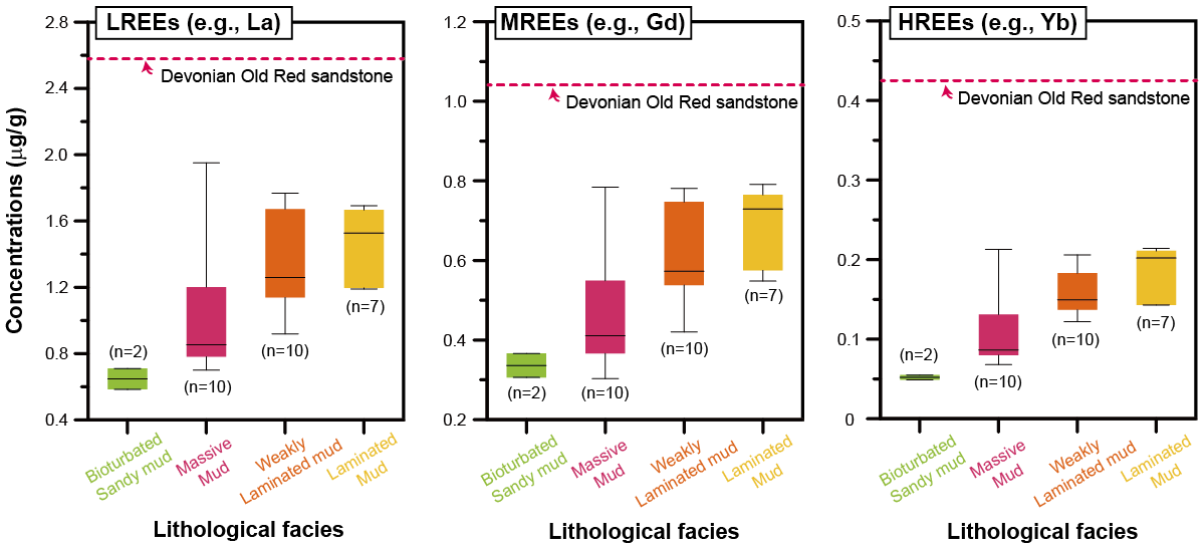

Fig. 3. Box and whisker plots of LREE (La), MREE (Gd) and HREE (Yb) concentrations in the leached authigenic phases of core 1085 in response to changes in lithological facies. The results in the leached weathering phases of the Devonian Old Red sandstone are also marked with pink dashed lines for comparison. The lithological facies, as defined by Jang et al. (2021), correspond to specific depth intervals: laminated mud (between 462-385 cm sediment depth), weakly laminated mud (385-228 cm), massive mud (228-30 cm) and bioturbated sandy mud (30-0 cm).

leached fraction of the Devonian Old Red sandstone is significantly greater than the range of Yb concentrations at Site 1085 (0.005 to 0.21 μg/g; average 0.14±0.05, 1 SD, n= 29). Finally, REE concentrations for leached fractions at Site 1085 exhibit some downcore variability, with concentrations being lower in the upper part (Fig. 3).

4.2. Previous results for Nd isotopes

The ε_{Nd} values for detrital and leached fractions of 1085 sediments have been previously discussed in Jang et al. (2021) and are briefly summarized here (Fig. 2). The detrital ε_{Nd} values range from -14.5 to -12.3, while leached fractions display slightly more radiogenic ε_{Nd} values between -13.6 and -10.4;the two fractions being strongly correlated with each other (r = 0.87, n = 29). In general, both ε_{Nd} values display larger variability in the laminated mud and weakly laminated mud facies, compared to the upper part of the core composed of massive mud and the bioturbated sandy mud facies.

The detrital ε_{Nd} values for the laminated mud facies at core 1085 are similar to those for surface sediments from central Woodfjorden (-14.1±0.2 from Jang et al., 2020) and the mouth of

Wijdefjorden (-14.2±0.2 from Jang et al., 2020), which are known to be directly sourced from the erosion of the Devonian Old Red sandstone. The laminated mud facies is also characterized by reddish sediment colour and relatively low dolomite contents (Fig. 2). Based on these observations, Jang et al. (2021) concluded that the Devonian Old Red sandstone from Woodfjorden and western Wijdefjorden was the main source of sediment in the section of core 1085, with probably minor contribution from Proterozoic metamorphic rocks in eastern Wijdefjorden (-25.4 to -18.6 from Johansson et al., 1995; Johansson and Gee, 1999). Conversely, an upward shift towards both more radiogenic detrital ε_{Nd} composition and higher dolomite contents was interpreted as reflecting enhanced sediment supply from Nordaustlandet (-13.2 to -7.4 from Johansson et al., 2000; Johansson et al., 2002). The relatively consistent ε_{Nd} values throughout the Holocene suggested a constant sediment provenance (Jang et al., 2021).

For the authigenic fractions, ε_{Nd} values at Site 1085 were generally less radiogenic than that for the Devonian Old Red sandstone (-10.8±0.2 from Jang et al., 2020), except for the bioturbated mud facies (Fig. 2). Jang et al. (2021) suggested leached Fe-(oxyhydr)oxides at Site 1085 mostly corresponded to authigenic oxides formed *in-situ* from either ambient seawater and/or meltwater rather than being directly sourced from eroded sedimentary rocks in glacial catchments.

The calculated $\triangle\varepsilon_{Nd}$ values indicated three prominent peaks during the late Holocene and at time intervals around 15.2 ka BP and 14.1 ka BP. These increased $\triangle\varepsilon_{Nd}$ values were interpreted as reflecting periods of glacial advance during which enhanced glacial abrasion increased the availability of fresh rock substrates and dissolution of poorly-resistant mineral phases (Jang et al., 2020). This process most likely caused greater Nd isotopic decoupling between solutes and source rocks (Hindshaw et al., 2018), hence resulting in higher $\triangle\varepsilon_{Nd}$ values (Jang et al., 2020).

214 **Table 1.** REE concentrations in leached phases of the Devonian Old Red Sandstone and sediments at site HH17-1085

Sample	Depth (cm)	La (µg/g)	Ce (µg/g)	Pr (µg/g)	Nd (µg/g)	Sm (µg/g)	Eu (µg/g)	Gd (µg/g)	Tb (µg/g)	Dy (µg/g)	Ho (µg/g)	Er (µg/g)	Tm (µg/g)	Yb (µg/g)	$(Gd/Yb)_N$	$(La/Gd)_N$	CI
HH17-1085-GC	0.5	0.710	1.766	0.210	0.925	0.235	0.058	0.366	0.044	0.186	0.034	0.078	0.011	0.055	3.86	0.27	3.81
	24.5	0.584	1.379	0.176	0.779	0.195	0.049	0.306	0.036	0.161	0.029	0.068	0.009	0.049	3.62	0.26	3.71
	49.5	0.700	1.458	0.191	0.819	0.194	0.049	0.303	0.037	0.173	0.032	0.085	0.012	0.068	2.58	0.32	2.83
	74.5	0.827	1.747	0.232	0.990	0.244	0.060	0.377	0.046	0.222	0.042	0.107	0.014	0.086	2.54	0.30	2.88
	99.5	0.781	1.706	0.219	0.960	0.235	0.059	0.366	0.044	0.212	0.040	0.099	0.014	0.077	2.76	0.29	3.04
	109.5	0.741	1.635	0.212	0.928	0.232	0.057	0.362	0.044	0.209	0.039	0.099	0.014	0.080	2.62	0.28	3.02
	124.5	0.847	1.871	0.239	1.047	0.257	0.064	0.404	0.048	0.233	0.043	0.108	0.015	0.087	2.69	0.29	3.03
	149.5	0.861	1.954	0.244	1.078	0.255	0.064	0.417	0.048	0.234	0.044	0.109	0.015	0.086	2.81	0.28	3.12
	174.5	0.927	2.125	0.261	1.141	0.278	0.068	0.444	0.053	0.254	0.048	0.123	0.018	0.098	2.63	0.29	2.99
	199.5	1.201	2.694	0.331	1.413	0.334	0.082	0.549	0.066	0.319	0.060	0.156	0.022	0.131	2.43	0.30	2.81
	224.5	1.559	3.278	0.419	1.762	0.418	0.097	0.679	0.081	0.389	0.072	0.189	0.026	0.154	2.56	0.32	2.82
	229.5	1.951	3.353	0.500	2.162	0.504	0.123	0.784	0.097	0.484	0.095	0.256	0.036	0.213	2.13	0.34	2.47
	239.5	1.138	2.542	0.317	1.351	0.329	0.077	0.538	0.063	0.304	0.056	0.149	0.020	0.122	2.56	0.29	2.93
	249.5	1.297	2.859	0.342	1.421	0.327	0.078	0.561	0.062	0.317	0.060	0.164	0.023	0.136	2.39	0.32	2.72
	274.5	1.672	3.768	0.461	1.936	0.457	0.112	0.758	0.089	0.424	0.081	0.220	0.031	0.183	2.40	0.30	2.78
	299.5	1.767	3.738	0.478	2.040	0.480	0.121	0.781	0.094	0.444	0.085	0.232	0.033	0.199	2.28	0.31	2.67
	324.5	1.688	3.594	0.470	1.957	0.458	0.120	0.747	0.090	0.445	0.083	0.226	0.034	0.206	2.10	0.31	2.56
	349.5	1.116	2.522	0.312	1.364	0.333	0.085	0.544	0.067	0.326	0.062	0.160	0.023	0.139	2.27	0.28	2.79
	359.5	1.300	2.886	0.361	1.512	0.366	0.092	0.595	0.073	0.360	0.067	0.179	0.026	0.157	2.20	0.30	2.66
	364.5	0.919	2.001	0.251	1.055	0.251	0.067	0.420	0.049	0.242	0.048	0.135	0.021	0.142	1.72	0.30	2.33
	369.5	1.222	2.707	0.352	1.488	0.370	0.092	0.585	0.071	0.349	0.067	0.184	0.026	0.161	2.11	0.29	2.66
	374.5	1.138	2.469	0.310	1.309	0.311	0.079	0.526	0.063	0.310	0.060	0.159	0.023	0.137	2.23	0.30	2.69
	389.5	1.527	3.308	0.446	1.901	0.472	0.121	0.729	0.090	0.437	0.084	0.225	0.032	0.203	2.08	0.29	2.64
	399.5	1.630	3.465	0.471	1.969	0.472	0.123	0.752	0.093	0.455	0.086	0.235	0.035	0.214	2.04	0.30	2.57
	409.5	1.509	3.248	0.423	1.744	0.409	0.100	0.674	0.081	0.397	0.072	0.197	0.029	0.182	2.15	0.31	2.60
	424.5	1.190	2.664	0.349	1.470	0.351	0.086	0.575	0.067	0.333	0.060	0.162	0.023	0.143	2.33	0.28	2.82
	434.5	1.196	2.654	0.339	1.390	0.331	0.082	0.548	0.065	0.309	0.058	0.159	0.024	0.143	2.22	0.30	2.68
	449.5	1.692	3.724	0.489	2.036	0.485	0.120	0.791	0.095	0.451	0.086	0.235	0.034	0.211	2.17	0.29	2.67
	459.5	1.667	3.634	0.471	1.962	0.453	0.117	0.765	0.091	0.438	0.083	0.225	0.032	0.202	2.20	0.30	2.67
080302*		2.579	2.579	6.459	0.771	4.622	1.075	0.222	1.041	0.117	0.815	0.120	0.432	0.050	0.425	0.34	1.99
WRAS†		37.8	77.7	8.77	32.69	6.15	1.188	5.19	0.819	4.95	1.019	2.97	-	3.01	-	-	-
UCC‡		30	64	7.1	26	4.5	0.88	3.8	0.64	3.5	0.8	2.3	0.33	2.2	1.00	1.08	0.96
NASC§		31.1	67.03	9.1	30.4	5.98	1.25	5.5	0.85	5.54	1.27	3.275	0.54	3.11	1.03	0.78	1.14

215 *Devonian Old Red sandstone collected from the Wood Bay Formation (79.39°N, 13.62°E; Jang et al., 2020)
216 †World River Average Silt (Bayon et al., 2015)
217 ‡Upper Continental Crust (McLennan, 2001; Taylor and McLennan, 1985)
218 §North American Shale Composite (Gromet et al., 1984)

5. Discussion

5.1. Pronounced MREE enrichments for sedimentary Fe-(oxyhydr)oxides in Svalbard

The corresponding shale-normalized REE patterns display MREE enrichments relative to light (LREE) and heavy REE (HREE) in both 1085 sediment samples and the Devonian Old Red sandstone (Fig. 4). The degree of MREE enrichment can be further visualized in a $(Gd/Yb)_N$ vs. $(La/Gd)_N$ diagram (Fig. 5). The calculated CI values of leached sediments at Site 1085 range from 2.3 to 3.8 (average CI ~ 2.8±0.3, 1 SD, n=29) (red squares in Fig. 5). These CI values are distinctively higher than that for the Devonian Old Red sandstone (~2.0) (white circle with red boundary in Fig. 5), indicating a strong MREE enrichment in core 1085 leachates compared to the leached Fe-(oxyhydr)oxide fraction associated with potential source rocks. This first observation, hence, intuitively suggests that leached sedimentary fractions at Site 1085 mostly correspond to authigenic Fe-(oxyhydr)oxides rather than pre-formed oxides of terrigenous origin (e.g., Bayon et al., 2004). This interpretation is thus consistent with inferences made from the use of ε_{Nd} values in both detrital and leached fractions (see also *section 4.2.*).

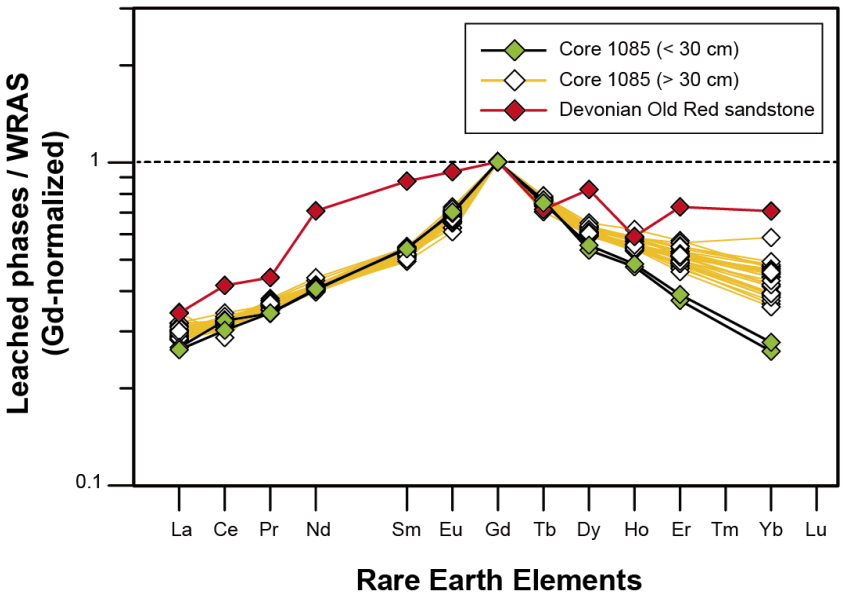

Fig. 4. Shale-normalized (WRAS; Bayon et al., 2020) REE patterns for the leached phases of core 1085 and the Devonian Old Red sandstone. The MREE enrichments are prevalent in core 1085, but more pronounced in bioturbated sandy mud facies (> 30 cm; green diamonds) compared to the other massive and laminated deposits (< 30 cm; white diamonds). Note that the REE data were also normalized by Gd_{WRAS} for clarity.

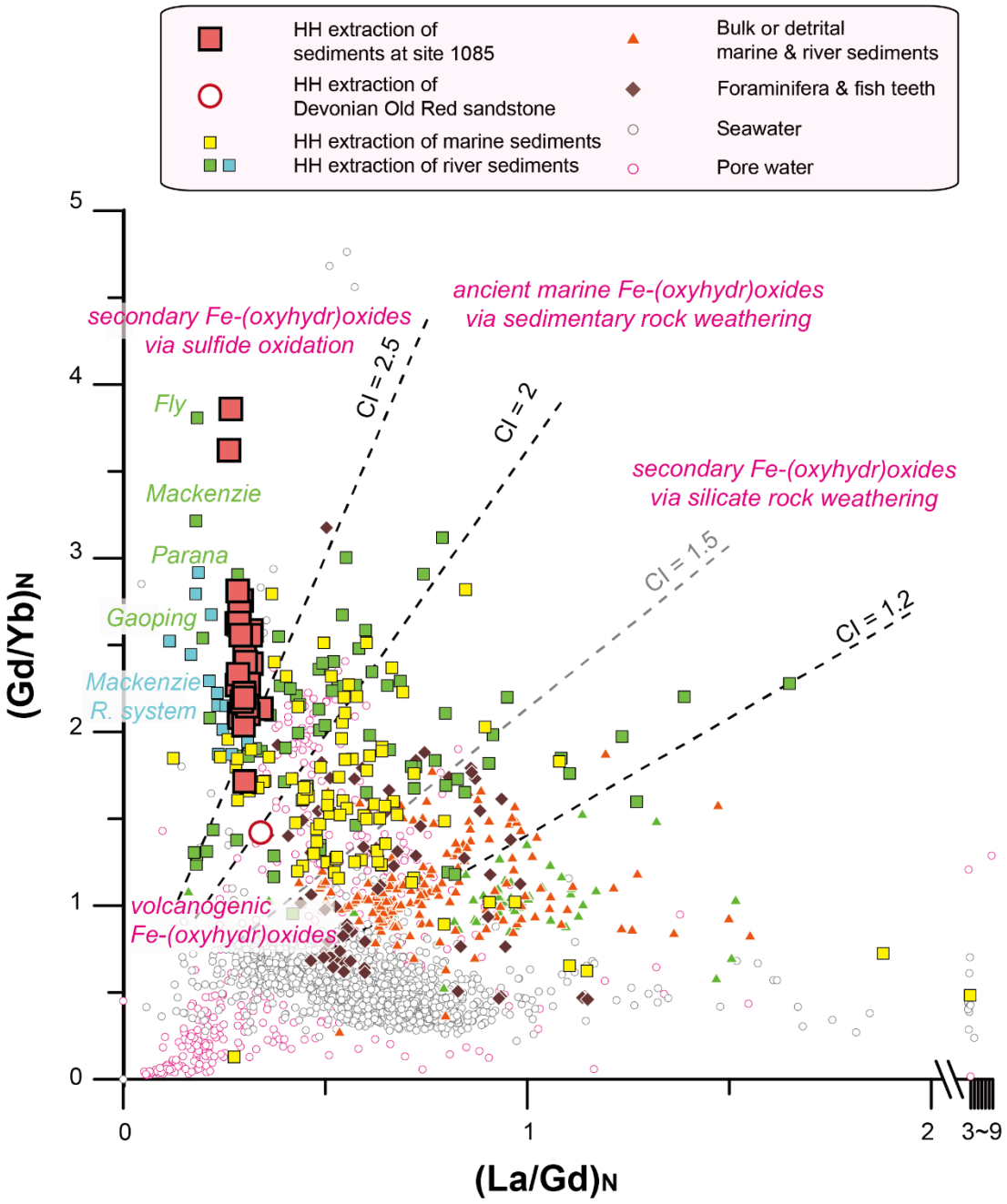

Fig. 5. Concavity index (CI) for the leached phases of marine sediments at Site 1085 and the Devonian Old Red sandstone. For comparison, the reported REE measurements from different archives such as the leached phases of marine and river sediments, bulk or residual marine and river sediments, foraminifers and fossil fish teeth and dissolved phases of seawater and porewater are marked with different symbols (for references, see Supplementary Table S1). Note that the leached riverine sediments collected from the Mackenzie River system (Larkin et al., 2021) are exclusively marked with sky blue squares.

233 Strikingly, our results indicate that the degree of MREE enrichment calculated in leached

234 authigenic phases at Site 1085 is higher than for typical authigenic phases extracted from marine

sediments. Dispersed Fe-(oxyhydr)oxide phases leached from marine sediments generally exhibit shale-normalized MREE enrichment patterns with an average CI of ~1.8±0.5 (1 SD, n=93; Basak et al., 2011; Bayon et al., 2002; Bayon et al., 2004; Blaser et al., 2016; Casse et al., 2019; Martin et al., 2010; Wilson et al., 2013; see yellow squares in Fig. 5). Likewise, REE measurements conducted on both bulk uncleaned foraminifers (which are thought to be controlled by the presence of authigenic Fe-Mn (oxyhydr)oxide coatings; Tachikawa et al., 2014) and fish teeth yield average CI values of ~ 1.2±0.3 (1 SD, n=43; Bayon et al., 2004; Blaser et al., 2016; Charbonnier et al., 2012; Molina-Kescher et al., 2014b; Skinner et al., 2019) and ~ 1.5±0.4 (1 SD, n=25; Martin et al., 2010), respectively, indicating moderate MREE enrichment (dark brown diamonds in Fig. 5). A similar average CI value of 1.2±0.5 (1 SD, n=391) is also generally encountered in pore waters (Abbott et al., 2015a; Bayon et al., 2011; Deng et al., 2017; Elderfield and Sholkovitz, 1987; Haley et al., 2004; Himmler et al., 2013; Kim et al., 2012; Sholkovitz et al., 1989; Sholkovitz et al., 1992; Soyol-Erdene and Huh, 2013; Yang J. et al., 2018; see white circles with pink boundaries in Fig. 5). Comparatively, fine-grained detrital sediments (average CI ~ 1.1±0.3, 1 SD, n=104; Bayon et al., 2015; see orange triangles in Fig. 5) and seawater (average CI ~ 1.0±0.3, 1 SD, n=1778; for references, see Supplementary Table S1; white circles with grey boundaries in Fig. 5) generally display no apparent MREE enrichment (i.e., CI values ~1).

In the marine environment, the MREE enrichment that typically characterizes leached authigenic phases is generally interpreted as reflecting the preferential incorporation of MREE over neighbouring REE by hydrogenous Fe-(oxyhydr)oxides (Martin et al., 2010) or the REE signature of upward-migrating reduced pore fluids from which early diagenetic Fe-(oxyhydr)oxides may precipitate at the sediment-seawater interface (Haley et al., 2004; Himmler et al., 2010; Skinner et al., 2019). However, the evidence that CI values at Site 1085 notably exceed by far those typically observed for leached marine sediments worldwide suggests that an additional mechanism comes into play to account for these anomalously high MREE enrichments in Fe-(oxyhydr)oxides from Svalbard glacimarine sediments.

5.2. High concavity index in sedimentary Fe-(oxyhydr)oxides as a proxy for sulfide weathering

Further insight into the potential cause of the high degree of MREE enrichment in Svalbard sedimentary Fe-(oxyhydr)oxides can be derived from the recent investigation of the corresponding phases in river sediments worldwide (Bayon et al., 2020) (green squares in Fig. 5). Like modern marine sediments, the leached fraction of river sediments also typically displays a characteristic MREE enrichment pattern (average CI ~ 2.1±0.6, 1 SD, n=74); however, their degree of MREE enrichment appears to be strongly dependent on the bedrock geology in corresponding drainage basins. While rivers draining sedimentary rocks and/or mixed lithologies tend to show pronounced MREE enrichments in leached sedimentary fractions with CI values generally >1.5, rivers draining crystalline silicate rocks generally display limited MREE enrichments with CI values ranging from 1.2 to ~2 (Bayon et al., 2020). The CI values of leached fractions of river sediments are largely set by the type of extracted Fe-(oxyhydr)oxide minerals (Bayon et al., 2020). For instance, in catchments dominated by marine sedimentary rocks, the erosion and subsequent transport of ancient seawater-derived mineral components represents a substantial source of sedimentary Fe-(oxyhydr)oxides with generally intermediate CI values between ~2 and 2.5. In contrast, in river basins dominated by crystalline igneous and metamorphic rocks, leached sediments mostly correspond to secondary Fe-(oxyhydr)oxides formed in soils during chemical weathering, thereby explaining their reduced degree of MREE enrichment (Bayon et al., 2020).

Consequently, the very high CI values (>2.5) observed in leached sedimentary fractions at Site 1085 are unlikely to be explained by the presence of pre-formed oxides related to the erosion of ancient marine sedimentary rocks and/or the alteration of silicate rocks on nearby continental regions (Fig. 5). It is important to re-emphasize here that the leached fraction of the studied Devonian Old Red sandstone has a CI value of ~2.0, and thus cannot account for the observed high CI values at Site 1085 (see also *section 5.1*).

In fact, Bayon et al. (2020) reported the occurrence of similarly high CI values >2.5 for a few leached fractions of river sediments derived from mountainous catchments dominated by sedimentary rock formations, such as the Fly (CI = 4.5), Mackenzie (4.1), Gaoping (3.5) and Parana (3.2) rivers

(Fig. 5). Additionally, recent work conducted on suspended river particulates from the Mackenzie River also reported pronounced MREE enrichments in leached fractions, yielding an average CI value of 3.2±0.6 (1 SD, n=14) (Larkin et al., 2021) (sky blue squares in Fig. 5). As mentioned in the Introduction, the fact that intense sulfide weathering has been identified as a major biogeochemical process in both the Mackenzie and Gaoping river catchments (Blattmann et al., 2019; Calmels et al., 2007), raised the possibility that such anomalously high MREE enrichments (with CI >2.5) could be possibly linked to the oxidation of pyrite or other sulfide minerals hosted in shales (Bayon et al., 2020).

A potential pitfall in this interpretation arises from the general lack of any particular MREE enrichment in common sulfide minerals such as pyrite, sphalerite, or galena (average CI ~ 1.1±0.5, 1 SD, n=16; Jiaxi et al., 2011), as well as in various mine-related deposits such as disseminated orebody waste, mine/industrial wastes, and minesoils (average CI ~ 0.9±0.2, 1 SD, n=52; Pérez-López et al., 2010) (Fig. 6). These data for both sulfide minerals and mining wastes suggest that the complete dissolution of sulfide minerals, i.e., indicative of congruent sulfide weathering, is unlikely to solely account for the anomalously high MREE enrichments observed in leached sedimentary Fe-(oxyhydr)oxides in Svalbard and certain river basins.

The precipitation of secondary Fe-(oxyhydr)oxide minerals following sulfide oxidation is given by the following equation:

$$FeS_2 + 15/4O_2 + 7/2H_2O \leftrightarrow Fe(OH)_3 + 2H_2SO_4$$

Iron (oxyhydr)oxide co-precipitation can result in preferential uptake of MREE (Martin et al., 2010). However, in the marine environment, leached Fe-(oxyhydr)oxide phases from sediments systematically display CI values below 2.5 (Fig. 5). Considering that both seawater (average CI ~ 1.0±0.3, 1 SD, n=1778; for references, see Supplementary Table S1) and sulfide minerals (average CI ~ 1.1±0.5, 1 SD, n=16; Jiaxi et al., 2011) display similar CI values, the REE decoupling induced by preferential uptake of MREE during iron co-precipitation is unlikely to explain CI values > 2.5 in Fe-(oxyhydr)oxides linked to sulfide oxidation. Alternatively, sulfuric acid, another byproduct of sulfide oxidation, could possibly play a role in driving the observed MREE enrichment. Following pyrite

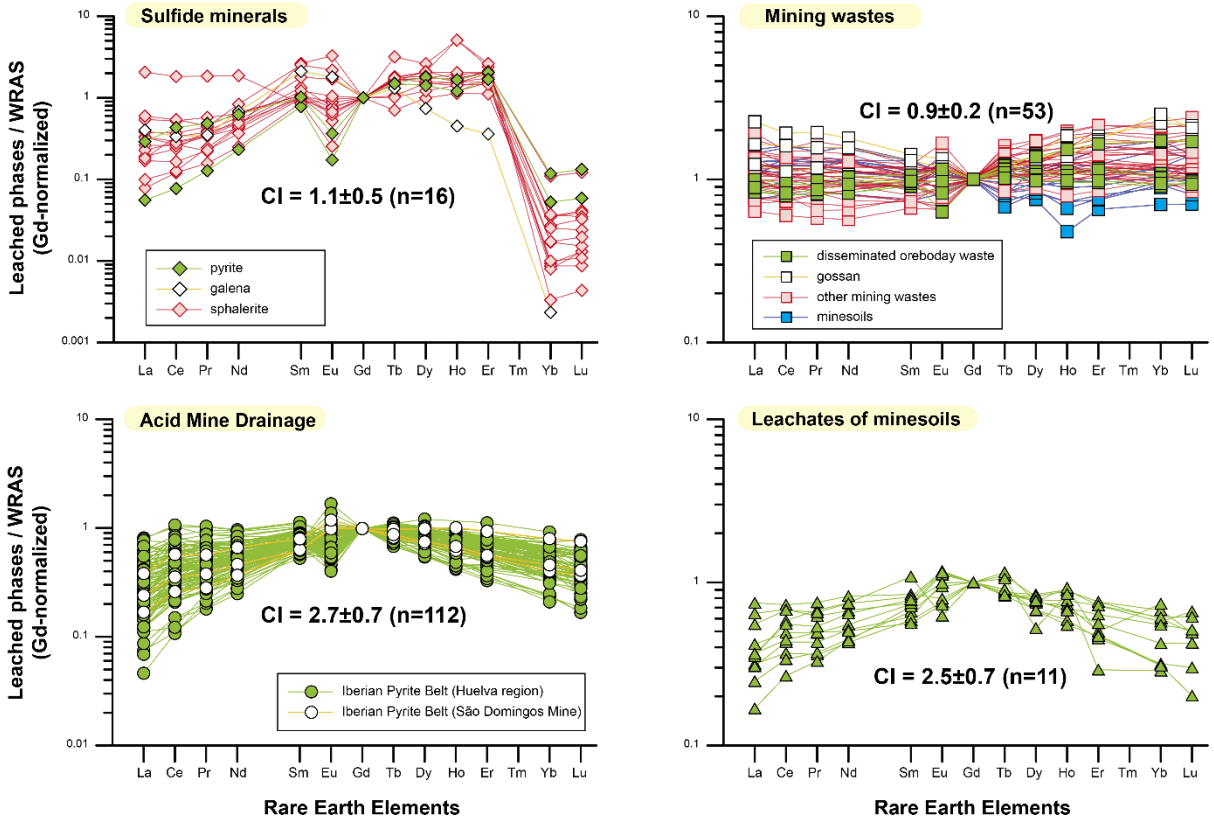

Fig. 6. Shale-normalized (WRAS; Bayon et al., 2020) REE patterns for sulfide minerals (Jiaxi et al., 2011), mining wastes (Pérez-López et al., 2010), Acid Mine Drainage (León et al., 2021; Pérez-López et al., 2010) and the leachates of minesoils (Pérez-López et al., 2010). Note that the REE data were also normalized by Gd_N for clarity.

316 oxidation, the release of sulfuric acid can significantly enhance the dissolution of rock-forming
317 minerals (Chigira and Oyama, 2000; Lerman and Wu, 2006). This mechanism can drive acid rock
318 drainage on continents (e.g., Konhauser et al., 2011), leading to preferential weathering of easily
319 dissolvable minerals such as apatite and carbonate (Langman et al., 2019; Lerman and Wu, 2006;
320 Takaya et al., 2015). Given the remarkably high MREE enrichment that typically characterizes
321 diagenetic apatite (average CI ~ 4.9±3.7, 1 SD, n=58; Ohr et al., 1994; Zhao et al., 2022), we suggest
322 that preferential alteration of MREE-enriched phosphate minerals, driven by sulfuric acid released
323 during sulfide oxidation, could possibly explain the observed high CI values in leached authigenic
324 fractions from Svalbard sediments.

325 Supporting evidence for the above hypothesis comes from REE data for acidic waters
326 released from metal or coal mining activities (i.e., acid mine drainage), which exhibit particularly high

MREE enrichments with CI values ranging from 1.8 to 5.1 (average CI ~ 2.7±0.7, 1 SD, n=112; León et al., 2021; Pérez-López et al., 2010) (Fig. 6). Similarly, the water exchangeable fraction of minesoils collected from the São Domingos mining area yielded high CI values ranging from 1.6 to 4.2 (average CI ~ 2.5±0.7, 1 SD, n=11; Pérez-López et al., 2010) (Fig. 6). Collectively, these observations suggest sulfide-driven chemical weathering can potentially account for MREE-enriched signatures in weathering products. The subsequent precipitation of Fe-(oxyhydr)oxides would further amplify the extent of MREE enrichment, possibly resulting in CI values exceeding 2.5 observed in leached sediments at Site 1085.

To some extent, this assumption is consistent with leaching experiments conducted on minesoils, where the highest CI values are encountered in samples displaying the highest levels of sulfate concentrations (Pérez-López et al., 2010) (Fig. 7). A similar relationship is also suspected in the Mackenzie River and its tributaries, as inferred from a general positive trend identified between the CI values for the leached fraction of suspended particulate material and dissolved sulfate concentrations in corresponding river waters (Larkin et al., 2021) (Fig. 7). While we acknowledge that further investigation would be needed to more thoroughly characterize the relationship between CI values and both sulfate/sulfide concentrations in aquatic environments, the sum of above observations provides empirical support for a link between high CI values and the degree of sulfide weathering, thereby further suggesting that pyrite oxidation may drive substantial MREE enrichment in sedimentary Fe-(oxyhydr)oxide phases.

5.3. Combined influences of sulfide weathering and early diagenesis on MREE enrichments in Svalbard sedimentary Fe(oxyhydr)oxides

The evidence presented above suggests that pyrite oxidation plays an important role in accounting for the pronounced MREE enrichment in leached Fe-(oxyhydr)oxide fractions at Site 1085. In (sub)Arctic environments and high-elevation regions worldwide, sulfide oxidation is generally viewed as the main biogeochemical reaction associated with glacial weathering (Torres et

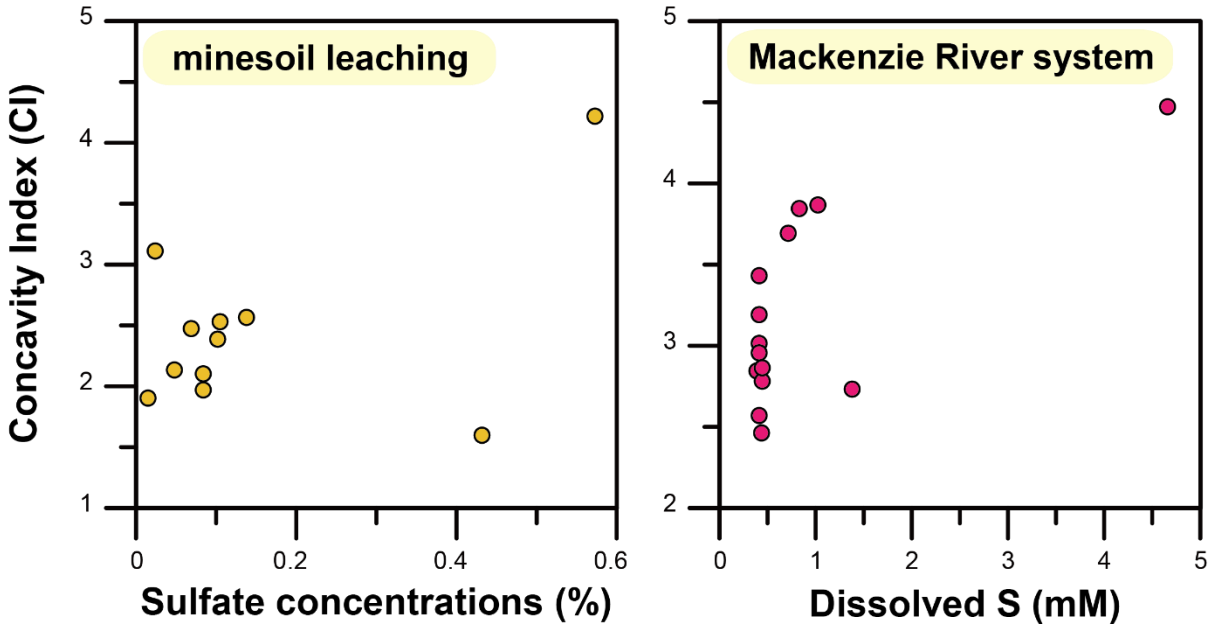

Fig. 7. General relationships between concavity index and dissolved SO_4^{2-} or S concentrations in the laboratory experiment and field study. Data from Pérez-López et al. (2010) and Larkin et al. (2021), respectively.

353 al., 2017; Wadham et al., 2019). Enhanced physical erosion by glacial abrasion typically results in
354 widespread exposure of reactive minerals such as iron sulfides on freshly-eroded rock substrates, thus
355 actively facilitating the process of oxidative sulfide weathering (Calmels et al., 2007; Stachnik et al.,
356 2022). Experimental studies also indicate that the very early stages of chemical weathering are
357 typically associated with the dissolution of apatite and other accessory minerals such as sphene, and
358 trace calcite (Bayon et al., 2006; Dausmann et al., 2019; Erel et al., 2004). This effect has been well
359 documented in young soils developed on glacial moraines (Harlavan et al., 2009). Taken together, the
360 above-mentioned evidence suggests that sulfuric acid released from sulfide oxidation in glacial
361 environments most likely contributes to the preferential dissolution of MREE-enriched apatite. As a
362 result, glacial meltwater can acquire a distinctive MREE-enriched signature that can be subsequently
363 incorporated into secondary Fe-(oxyhydr)oxides upon precipitation (see also *section 5.2*).
364 In Svalbard, huge amounts of nanoparticulate iron minerals formed in glaciated catchments
365 are transported to the proximal marine environment via glacial meltwater runoff (e.g., Herbert et al.,
366 2020). This important influx of nanoparticulate Fe promotes intense marine productivity and
367 subsequent deposition of Fe-(oxyhydr)oxide minerals (Jang et al., 2023; Zhang et al., 2015). Once

368 buried, the rapid accumulation of organic matter and reactive iron-bearing phases in glacimarine
369 sediments drives intense diagenetic processes such as dissimilatory iron reduction and sulfate
370 reduction. This pool of reactive glacially-derived iron can also potentially serve as a primary oxidant
371 for dissolved sulfide released during sulfate reduction, thereby regulating the rate of sulfide oxidation
372 in pore waters (Findlay et al., 2020; Michaud et al., 2020). These coupled Fe and S cycles have been
373 widely investigated in Svalbard fjords (Herbert et al., 2020, 2022; Laufer-Meiser et al., 2021;
374 Michaud et al., 2020; Wehrmann et al., 2014, 2017). All these intense diagenetic reactions taking
375 place in glacimarine sediments could potentially play a role in the observed MREE enrichments in
376 leached authigenic fractions at Site 1085. Presumably, early diagenetic reduction of glacially-derived
377 MREE-enriched Fe-(oxyhydr)oxides in Svalbard sediments is likely accompanied by a pronounced
378 MREE enrichment in surrounding interstitial waters (e.g., Haley et al., 2004). Upon upward diffusive
379 migration of MREE-enriched fluids, *in-situ* precipitation of hydrogenous Fe-(oxyhydr)oxides at the
380 oxic surface sediment interface could represent an additional mechanism explaining the acquisition of
381 particularly high CI values in leached sedimentary fractions. Future investigation of pore waters and
382 sediments will be required to provide additional insights into the impact of early diagenetic processes
383 on REE cycling in Svalbard.
384
385 *5.4. Interpretation of the Holocene authigenic REE record at Site 1085*
386 Based on the above findings, we explore below the potential factors explaining the observed
387 variability of CI values in leached sedimentary fractions at Site 1085. Core 1085 indicate two distinct
388 intervals characterized by different CI values (Fig. 8). The late Holocene sediment interval exhibits an
389 average CI value of 3.8±0.1 (1 SD, n=2), while the earlier interval displays comparatively lower CI
390 values with an average of 2.8±0.2 (1 SD, n=27) (Fig. 8). Measurements of Nd isotope ratios in detrital
391 fractions at Site 1085 indicate a similar provenance across the middle-to-late Holocene transition
392 (Jang et al., 2021), thereby suggesting that the observed shift in CI values in leached fractions is
393 unlikely to reflect a change in sediment provenance (Fig. 8). Alternatively, the observed shift in CI
394 values at Site 1085 could be interpreted as reflecting more intense pyrite oxidation during the late

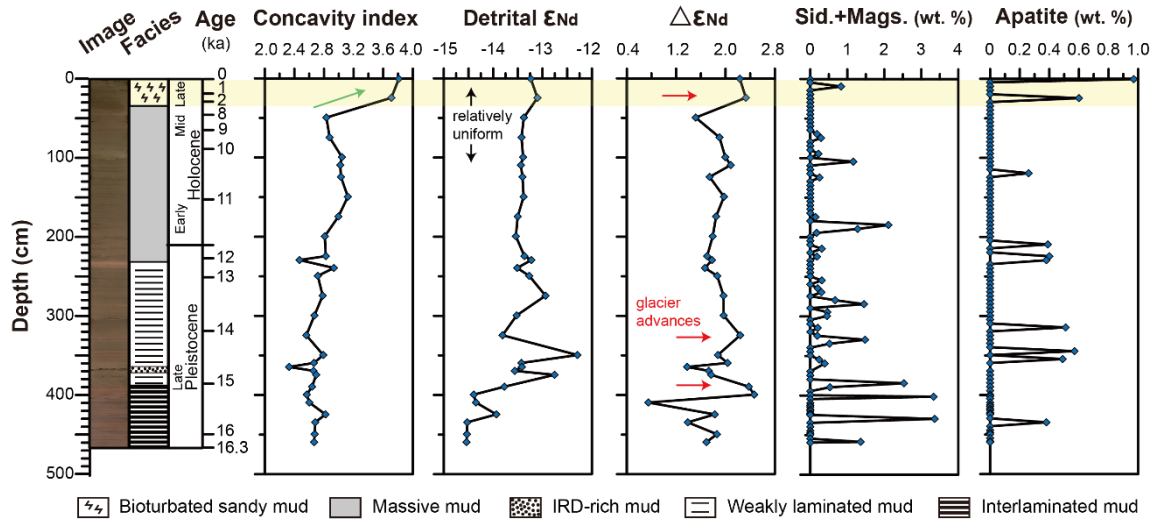

Fig. 8. Temporal variability of concavity index estimated from core 1085. Proxies for sediment provenance (detrital ε_{Nd}) and glacial advances ($\triangle\varepsilon_{Nd}$) are also included for comparison (Jang et al., 2021). In addition, bulk mineral compositions, including the sum of siderite (sid.) and magnesite (mags.), and apatite (Vogt and Jang, 2023), are presented.

Holocene. For instance, the late Holocene glacier advance in northern Svalbard (Jang et al., 2021) could have promoted preferential alteration of reactive sulfide minerals and other accessory minerals (including apatite) on newly eroded rock substrates (e.g., Gutjahr et al., 2009; Jang et al., 2020; Vance et al., 2009). However, the absence of any CI increase at 15.1 and 14.3 ka, i.e., at periods when glacier re-advances are known to have taken place in this region (Jang et al., 2021 and see also *section 4.2.*) (Fig. 8), makes this hypothesis unlikely. Nevertheless, the last deglaciation (16.3 to 12.1 ka) is a period characterized by significant variability in sediment provenance as well as an overall trend of glacier retreat in northern Svalbard, despite episodic glacier re-advances (Jang et al., 2021) (Fig. 8). In light of this complicated deglacial environmental context, we recognize that the significance of CI values for tracing ice sheet dynamics and identifying periods of past glacier advances and associated increase of sulfide weathering in the sedimentary record remains unclear and should deserve further investigation.

Instead, early diagenetic Fe cycling in Svalbard sediments could possibly explain the late Holocene shift towards high CI values in leached authigenic fractions at Site 1085. This interpretation

409 is supported by the observation that the highest CI values are exclusively found within the bioturbated
410 and presumably oxic sandy mud facies in the uppermost sediment horizon (Fig. 8). As discussed
411 above, co-precipitation of authigenic Fe-(oxyhydr)oxides at the sediment-seawater interface (e.g.,
412 Laufer-Meiser et al., 2021) would represent a plausible mechanism accounting for the highest CI
413 values measured at Site 1085. In addition to Fe-(oxyhydr)oxides, early diagenetic precipitation of
414 other authigenic mineral phases such as siderite and apatite could also represent additional sinks for
415 MREE in oxic sediment layers (e.g., Ohr et al., 1994; Rongemaille et al., 2011; Zhao et al., 2022),
416 although their downcore distribution at Site 1085 does not provide strong support for this hypothesis
417 (Fig. 8).

418 Finally, it is possible that enhanced sulfide weathering during the most recent period was
419 linked to mining activity. Coal mining activity in Svalbard has been in operation since the early
420 1900s, and its environmental impact on the fjord and coastal regions has been well-documented using
421 various tracers such as heavy metals, radionuclides, and polycyclic aromatic hydrocarbons (e.g.,
422 Askaer et al., 2008; Dowdall et al., 2004; Lee et al., 2023). By analogy with the observation of
423 pronounced MREE enrichments in acid mine drainage (León et al., 2021; Pérez-López et al., 2010),
424 mining activity in Svalbard and its hydrological impact on marine fjord environments could possibly
425 explain, at least partly, the shift towards higher CI values in the upper sediment record at Site 1085.
426 Nevertheless, mining activities in Svalbard have been implemented in regions around Isfjorden
427 (Longyearbyen, Pyramiden and Barentsburg), Kongsfjorden (Ny-Ålesund), and Van Mijenfjorden
428 (Sveagruva) (Fig. 1), hence relatively far from Site 1085; a substantial impact of mining activity on
429 Site 1085 sedimentation thus appears unlikely.

430 Collectively, the significant MREE enrichment observed in leached sedimentary fractions at
431 Site 1085 suggests that high sulfide weathering fluxes have been prevalent in Svalbard since the last
432 deglaciation, primarily driven by glacial weathering. During the late Holocene, the highest CI values
433 observed could possibly relate to early diagenetic processes, although enhanced sulfide oxidation
434 following widespread glacial advance in Svalbard during this period could have also played a role.
435

6. Conclusions and perspectives

In this study, we have analysed glacimarine sediments recovered from the northern Svalbard continental shelf in the Arctic Ocean to investigate whether REE abundances in sedimentary Fe-(oxyhydr)oxide phases can be used for tracing 'glacial' chemical weathering patterns. We show that leached Fe-(oxyhydr)oxide fractions in Svalbard glacimarine sediments deposited over the last 16.3 ka exhibit distinctive shale-normalized REE patterns characterized by pronounced mid-REE enrichments (as inferred from the use of the so-called 'concavity index'; CI), much higher than previously encountered in any other marine environments. By analogy with a similar degree of MREE enrichment previously reported in acid mine drainage and minesoil leachates as well as in leached Fe-(oxyhydr)oxide fractions of river sediments from catchments dominated by sulfide weathering, we argue that the pronounced MREE enrichment observed in leached Svalbard sediments (CI > 2.5) links to predominant oxidative sulfide weathering in corresponding catchment areas. While the exact mechanism of such MREE enrichment remains unclear, we suggest that the release of sulfuric acid following glacial erosion and enhanced sulfide oxidation could result in preferential alteration of MREE-enriched mineral phases such as apatite. The resulting REE signature released in glacial meltwaters could be subsequently incorporated into glacially-derived Fe-(oxyhydr)oxide phases during precipitation in surface environments. Early diagenetic reduction of Fe-(oxyhydr)oxide phases buried in sediments, followed by subsequent precipitation of hydrogenous Fe-(oxyhydr)oxide at the sediment-seawater interface, could represent an additional mechanism explaining significant authigenic MREE enrichment in Svalbard sediments. As cryospheric regions are currently diminishing due to ongoing global warming, authigenic REE records in glacimarine systems under various hydrological settings (e.g., land vs. marine-terminating glaciers) could provide a promising tool to investigate combined biogeochemical sulfur and iron cycling in polar environments. Furthermore, our study highlights the potential interest of using authigenic REE in deep-time sedimentary records in order to investigate the evolution of oxidative sulfide weathering over geological timescales and its role as an oxygen sink or a source of carbon dioxide to the Earth's atmosphere.

462

463 **Data Availability**

464 Datasets related to this article can be found in Table 1.

465

466 **Acknowledgements**

467 This study was supported mainly by the Basic Core Technology Development Program for the
468 Oceans and the Polar Regions (NRF-2021M1A5A1075512) from the NRF funded by MSIT, Republic
469 of Korea. Additionally, this research was partly supported by the Basic Science Research Program of
470 National Research Foundation of Korea (NRF-2017R1A6A1A07015374). We would like to thank all
471 the participants of the cruises on RV *Helmer Hanssen* for their support of the core sampling, as well as
472 D. Kim and Y. Son for laboratory assistance. Lastly, we express our gratitude to the Editor, Christian
473 France-Lanord, and to the anonymous reviewers for their highly valuable and constructive feedbacks
474 on this manuscript.

475

476 **References .**

477 Abbott, A.N., Haley, B.A., McManus, J., 2015a. Bottoms up: Sedimentary control of the deep North
478 Pacific Ocean's ε_{Nd} signature. Geology 43, 1035-1035.
479 Abbott, A.N., Haley, B.A., McManus, J., Reimers, C.E., 2015b. The sedimentary flux of dissolved
480 rare earth elements to the ocean. Geochim. Cosmochim. Acta 154, 186-200.
481 Alibo, D.S., Nozaki, Y., 1999. Rare earth elements in seawater: particle association, shale-
482 normalization, and Ce oxidation. Geochim. Cosmochim. Acta 63, 363-372.
483 Allaart, L., Müller, J., Schomacker, A., Rydningen, T.A., Håkansson, L., Kjellman, S.E., Mollenhauer,
484 G., Forwick, M., 2020. Late Quaternary glacier and sea-ice history of northern Wijdefjorden,
485 Svalbard. Boreas, doi:10.1111/bor.12435.
486 Amakawa, H., Alibo, D.S., Nozaki, Y., 2000. Nd isotopic composition and REE pattern in the surface
487 waters of the eastern Indian Ocean and its adjacent seas. Geochim. Cosmochim. Acta 64,
488 1715-1727.
489 Anderson, S.P., Drever, J.I., Frost, C.D., Holden, P., 2000. Chemical weathering in the foreland of a
490 retreating glacier. Geochim. Cosmochim. Acta 64, 1173-1189.
491 Askaer, L., Schmidt, L.B., Elberling, B., Asmund, G., Jónsdóttir, I.S., 2008. Environmental impact on
492 an Arctic soil–plant system resulting from metals released from coal mine waste in Svalbard
493 (78°N). Water Air Soil Pollut. 195, 99-114.
494 Basak, C., Martin, E.E., Kamenov, G.D., 2011. Seawater Pb isotopes extracted from Cenozoic marine
495 sediments. Chem. Geol. 286, 94-108.
496 Bayon, G., Barrat, J.A., Etoubleau, J., Benoit, M., Bollinger, C., Révillon, S., 2009. Determination of
497 rare earth elements, Sc, Y, Zr, Ba, Hf and Th in geological samples by ICP-MS after Tm
498 addition and alkaline fusion. Geostand. Geoanal. Res. 33, 51-62.
499 Bayon, G., Birot, D., Ruffine, L., Caprais, J.C., Ponzevera, E., Bollinger, C., Donval, J.P., Charlou,
500 J.L., Voisset, M., Grimaud, S., 2011. Evidence for intense REE scavenging at cold seeps from
501 the Niger Delta margin. Earth Planet. Sci. Lett. 312, 443-452.
502 Bayon, G., German, C.R., Boella, R.M., Milton, J.A., Taylor, R.N., Nesbitt, R.W., 2002. An improved

503 method for extracting marine sediment fractions and its application to Sr and Nd isotopic
504 analysis. Chem. Geol. 187, 179-199.
505 Bayon, G., German, C.R., Burton, K.W., Nesbitt, R.W., Rogers, N., 2004. Sedimentary Fe-Mn
506 oxyhydroxides as paleoceanographic archives and the role of aeolian flux in regulating
507 oceanic dissolved REE. Earth Planet. Sci. Lett. 224, 477-492.
508 Bayon, G., Lambert, T., Vigier, N., De Deckker, P., Freslon, N., Jang, K., Larkin, C.S., Piotrowski,
509 A.M., Tachikawa, K., Thollon, M., Tipper, E.T., 2020. Rare earth element and neodymium
510 isotope tracing of sedimentary rock weathering. Chem. Geol. 553, 119794.
511 Bayon, G., Toucanne, S., Skonieczny, C., Andre, L., Bermell, S., Cheron, S., Dennielou, B.,
512 Etoubleau, J., Freslon, N., Gauchery, T., Germain, Y., Jorry, S.J., Menot, G., Monin, L.,
513 Ponzevera, E., Rouget, M.L., Tachikawa, K., Barrat, J.A., 2015. Rare earth elements and
514 neodymium isotopes in world river sediments revisited. Geochim. Cosmochim. Acta 170, 17-
515 38.
516 Bayon, G., Vigier, N., Burton, K.W., Brenot, A., Carignan, J., Etoubleau, J., Chu, N.-C., 2006. The
517 control of weathering processes on riverine and seawater hafnium isotope ratios. Geology 34,
518 433-436.
519 Behrens, M.K., Pahnke, K., Paffrath, R., Schnetger, B., Brumsack, H.-J., 2018. Rare earth element
520 distributions in the West Pacific: Trace element sources and conservative vs. non-conservative
521 behavior. Earth Planet. Sci. Lett. 486, 166-177.
522 Blaser, P., Lippold, J., Gutjahr, M., Frank, N., Link, J.M., Frank, M., 2016. Extracting foraminiferal
523 seawater Nd isotope signatures from bulk deep sea sediment by chemical leaching. Chem.
524 Geol. 439, 189-204.
525 Blattmann, T.M., Wang, S.-L., Lupker, M., Märki, L., Haghipour, N., Wacker, L., Chung, L.-H.,
526 Bernasconi, S.M., Plötze, M., Eglinton, T.I., 2019. Sulphuric acid-mediated weathering on
527 Taiwan buffers geological atmospheric carbon sinks. Sci. Rep. 9, 2945.
528 Böhm, E., Lippold, J., Gutjahr, M., Frank, M., Blaser, P., Antz, B., Fohlmeister, J., Frank, N.,
529 Andersen, M., Deininger, M., 2015. Strong and deep Atlantic meridional overturning

circulation during the last glacial cycle. Nature 517, 73-76.

Calmels, D., Gaillardet, J., Brenot, A., France-Lanord, C., 2007. Sustained sulfide oxidation by physical erosion processes in the Mackenzie River basin: Climatic perspectives. Geology 35, 1003-1006.

Casse, M., Montero-Serrano, J.-C., St-Onge, G., Poirier, A., 2019. REE distribution and Nd isotope composition of estuarine waters and bulk sediment leachates tracing lithogenic inputs in eastern Canada. Mar. Chem. 211, 117-130.

Charbonnier, G., Pucéat, E., Bayon, G., Desmares, D., Dera, G., Durlet, C., Deconinck, J.-F., Amédro, F., Gourlan, A.T., Pellenard, P., 2012. Reconstruction of the Nd isotope composition of seawater on epicontinental seas: Testing the potential of Fe–Mn oxyhydroxide coatings on foraminifera tests for deep-time investigations. Geochim. Cosmochim. Acta 99, 39-56.

Chigira, M., Oyama, T., 2000. Mechanism and effect of chemical weathering of sedimentary rocks, in: Kanaori, Y., Tanaka, K., Chigira, M. (Eds.), Developments in Geotechnical Engineering. Elsevier, pp. 267-278.

Dallmann, W., Elvevold, S., 2015. Bedrock Geology. Geoscience Atlas of Svalbard, Norsk Polarinstitutt, Tromsø 148, 133-173.

Dausmann, V., Gutjahr, M., Frank, M., Kouzmanov, K., Schaltegger, U., 2019. Experimental evidence for mineral-controlled release of radiogenic Nd, Hf and Pb isotopes from granitic rocks during progressive chemical weathering. Chem. Geol. 507, 64-84.

Deng, Y., Ren, J., Guo, Q., Cao, J., Wang, H., Liu, C., 2017. Rare earth element geochemistry characteristics of seawater and porewater from deep sea in western Pacific. Sci. Rep. 7, 16539.

Dias, B.B., Piotrowski, A.M., Barbosa, C.F., Venancio, I.M., Chiessi, C.M., Albuquerque, A.L.S., 2021. Coupled changes in western South Atlantic carbon sequestration and particle reactive element cycling during millennial-scale Holocene climate variability. Sci. Rep. 11, 24378.

Dowdall, M., Vicat, K., Frearson, I., Gerland, S., Lind, B., Shaw, G., 2004. Assessment of the radiological impacts of historical coal mining operations on the environment of Ny-Ålesund, Svalbard. J. Environ. Radioactiv. 71, 101-114.

557 Elderfield, H., Sholkovitz, E.R., 1987. Rare earth elements in the pore waters of reducing nearshore
558 sediments. Earth Planet. Sci. Lett. 82, 280-288.
559 Erel, Y., Blum, J.D., Roueff, E., Ganor, J., 2004. Lead and strontium isotopes as monitors of
560 experimental granitoid mineral dissolution. Geochim. Cosmochim. Acta 68, 4649-4663.
561 Farnsworth, W.R., Allaart, L., Ingólfsson, Ó., Alexanderson, H., Forwick, M., Noormets, R., Retelle,
562 M., Schomacker, A., 2020. Holocene glacial history of Svalbard: Status, perspectives and
563 challenges. Earth-Sci. Rev. 208, 103249.
564 Findlay, A.J., Pellerin, A., Laufer, K., Jørgensen, B.B., 2020. Quantification of sulphide oxidation
565 rates in marine sediment. Geochim. Cosmochim. Acta 280, 441-452.
566 Flink, A.E., Noormets, R., Fransner, O., Hogan, K.A., ÓRegan, M., Jakobsson, M., 2017. Past ice
567 flow in Wahlenbergfjorden and its implications for late Quaternary ice sheet dynamics in
568 northeastern Svalbard. Quat. Sci. Rev. 163, 162-179.
569 Forwick, M., Vorren, T.O., 2009. Late Weichselian and Holocene sedimentary environments and ice
570 rafting in Isfjorden, Spitsbergen. Palaeogeogr. Palaeoclimatol. Palaeoecol. 280, 258-274.
571 Frank, M., 2002. Radiogenic isotopes: tracers of past ocean circulation and erosional input. Rev.
572 Geophys. 40, 1-1-1-38.
573 Garcia-Solsona, E., Jeandel, C., Labatut, M., Lacan, F., Vance, D., Chavagnac, V., Pradoux, C., 2014.
574 Rare earth elements and Nd isotopes tracing water mass mixing and particle-seawater
575 interactions in the SE Atlantic. Geochim. Cosmochim. Acta 125, 351-372.
576 German, C.R., Elderfield, H., 1989. Rare earth elements in Saanich Inlet, British Columbia, a
577 seasonally anoxic basin. Geochim. Cosmochim. Acta 53, 2561-2571.
578 German, C.R., Holliday, B.P., Elderfield, H., 1991. Redox cycling of rare earth elements in the
579 suboxic zone of the Black Sea. Geochim. Cosmochim. Acta 55, 3553-3558.
580 Grasse, P., Bosse, L., Hathorne, E.C., Böning, P., Pahnke, K., Frank, M., 2017. Short-term variability
581 of dissolved rare earth elements and neodymium isotopes in the entire water column of the
582 Panama Basin. Earth Planet. Sci. Lett. 475, 242-253.
583 Greaves, M.J., Elderfield, H., Sholkovitz, E.R., 1999. Aeolian sources of rare earth elements to the

584 Western Pacific Ocean. Mar. Chem. 68, 31-38.
585 Grenier, M., Jeandel, C., Lacan, F., Vance, D., Venchiarutti, C., Cros, A., Cravatte, S., 2013. From the
586 subtropics to the central equatorial Pacific Ocean: Neodymium isotopic composition and rare
587 earth element concentration variations. J. Geophys. Res. Oceans 118, 592-618.
588 Gromet, L.P., Haskin, L.A., Korotev, R.L., Dymek, R.F., 1984. The "North American shale
589 composite": Its compilation, major and trace element characteristics. Geochim. Cosmochim.
590 Acta 48, 2469-2482.
591 Gutjahr, M., Frank, M., Halliday, A.N., Keigwin, L.D., 2009. Retreat of the Laurentide ice sheet
592 tracked by the isotopic composition of Pb in western North Atlantic seawater during
593 termination 1. Earth Planet. Sci. Lett. 286, 546-555.
594 Haley, B.A., Frank, M., Hathorne, E., Pisias, N., 2014. Biogeochemical implications from dissolved
595 rare earth element and Nd isotope distributions in the Gulf of Alaska. Geochim. Cosmochim.
596 Acta 126, 455-474.
597 Haley, B.A., Klinkhammer, G.P., McManus, J., 2004. Rare earth elements in pore waters of marine
598 sediments. Geochim. Cosmochim. Acta 68, 1265-1279.
599 Harlavan, Y., Erel, Y., Blum, J.D., 2009. The coupled release of REE and Pb to the soil labile pool
600 with time by weathering of accessory phases, Wind River Mountains, WY. Geochim.
601 Cosmochim. Acta 73, 320-336.
602 Hathorne, E.C., Stichel, T., Brück, B., Frank, M., 2015. Rare earth element distribution in the Atlantic
603 sector of the Southern Ocean: The balance between particle scavenging and vertical supply.
604 Mar. Chem. 177, 157-171.
605 Herbert, L.C., Michaud, A.B., Laufer-Meiser, K., Hoppe, C.J.M., Zhu, Q., Aller, R.C., Jørgensen,
606 B.B., Wehrmann, L.M., 2022. Tight benthic-pelagic coupling drives seasonal and interannual
607 changes in iron-sulfur cycling in Arctic fjord sediments (Kongsfjorden, Svalbard). J. Marine
608 Syst. 225, 103645.
609 Herbert, L.C., Riedinger, N., Michaud, A.B., Laufer, K., Røy, H., Jørgensen, B.B., Heilbrun, C., Aller,
610 R.C., Cochran, J.K., Wehrmann, L.M., 2020. Glacial controls on redox-sensitive trace element

611 cycling in Arctic fjord sediments (Spitsbergen, Svalbard). Geochim. Cosmochim. Acta 271,
612 33-60.
613 Himmler, T., Bach, W., Bohrmann, G., Peckmann, J., 2010. Rare earth elements in authigenic
614 methane-seep carbonates as tracers for fluid composition during early diagenesis. Chem. Geol.
615 277, 126-136.
616 Himmler, T., Haley, B.A., Torres, M.E., Klinkhammer, G.P., Bohrmann, G., Peckmann, J., 2013. Rare
617 earth element geochemistry in cold-seep pore waters of Hydrate Ridge, northeast Pacific
618 Ocean. Geo-Mar. Lett. 33, 369-379.
619 Hindshaw, R.S., Aciego, S.M., Piotrowski, A.M., Tipper, E.T., 2018. Decoupling of dissolved and
620 bedrock neodymium isotopes during sedimentary cycling. Geochem. Perspect. Lett. 8, 43-46.
621 Hughes, A.L., Gyllencreutz, R., Lohne, Ø.S., Mangerud, J., Svendsen, J.I., 2016. The last Eurasian ice
622 sheets–a chronological database and time-slice reconstruction, DATED-1. Boreas 45, 1-45.
623 Jacobsen, S.B., Wasserburg, G.J., 1980. Sm-Nd isotopic evolution of chondrites. Earth Planet. Sci.
624 Lett. 50, 139-155.
625 Jakobsson, M., Mayer, L.A., Bringensparr, C., Castro, C.F., Mohammad, R., Johnson, P., Ketter, T.,
626 Accettella, D., Amblas, D., An, L., Arndt, J.E., Canals, M., Casamor, J.L., Chauché, N.,
627 Coakley, B., Danielson, S., Demarte, M., Dickson, M.-L., Dorschel, B., Dowdeswell, J.A.,
628 Dreutter, S., Fremand, A.C., Gallant, D., Hall, J.K., Hehemann, L., Hodnesdal, H., Hong, J.,
629 Ivaldi, R., Kane, E., Klaucke, I., Krawczyk, D.W., Kristoffersen, Y., Kuipers, B.R., Millan, R.,
630 Masetti, G., Morlighem, M., Noormets, R., Prescott, M.M., Rebesco, M., Rignot, E.,
631 Semiletov, I., Tate, A.J., Travaglini, P., Velicogna, I., Weatherall, P., Weinrebe, W., Willis, J.K.,
632 Wood, M., Zarayskaya, Y., Zhang, T., Zimmermann, M., Zinglersen, K.B., 2020. The
633 International Bathymetric Chart of the Arctic Ocean Version 4.0. Sci. Data 7, 176.
634 Jang, K., Ahn, Y., Joe, Y.J., Braun, C.A., Joo, Y.J., Kim, J.-H., Bayon, G., Forwick, M., Vogt, C., Nam,
635 S.-I., 2021. Glacial and environmental changes in northern Svalbard over the last 16.3 ka
636 inferred from neodymium isotopes. Glob. Planet. Chang. 201, 103483.
637 Jang, K., Bayon, G., Han, Y., Joo, Y.J., Kim, J.-H., Ryu, J.-S., Woo, J., Forwick, M., Szczuciński, W.,

638 Kim, J.-H., Nam, S.-I., 2020. Neodymium isotope constraints on chemical weathering and past
639 glacial activity in Svalbard. Earth Planet. Sci. Lett. 542, 116319.
640 Jang, K., Bayon, G., Vogt, C., Forwick, M., Ahn, Y., Kim, J.-H., Nam, S.-I., 2023. Non-linear
641 response of glacier melting to Holocene warming in Svalbard recorded by sedimentary iron
642 (oxyhydr)oxides. Earth Planet. Sci. Lett. 607, 118054.
643 Jang, K., Huh, Y., Han, Y., 2017. Authigenic Nd isotope record of North Pacific Intermediate Water
644 formation and boundary exchange on the Bering Slope. Quat. Sci. Rev. 156, 150-163.
645 Jeandel, C., Delattre, H., Grenier, M., Pradoux, C., Lacan, F., 2013. Rare earth element concentrations
646 and Nd isotopes in the Southeast Pacific Ocean. Geochem. Geophys. Geosyst. 14, 328-341.
647 Jiaxi, Z., Zhilong, H., Guofu, Z., Xiaobiao, L., Wei, D., Guangping, B., 2011. Trace elements and rare
648 earth elements of sulfide minerals in the Tianqiao Pb-Zn ore deposit, Guizhou Province,
649 China. Acta Geol. Sin.-Engl. 85, 189-199.
650 Joe, Y.J., Jang, K., Forwick, M., Laberg, J.S., Kong, G.S., Kang, M.-H., Yoon, S.-H., Nam, S.-I.,
651 2022. Glacial history and depositional environments in little Storfjorden and Hambergbukta of
652 Arctic Svalbard since the younger dryas. Front. Earth Sci. 10.
653 Johansson, Å., Gee, D., Björklund, L., Witt-Nilsson, P., 1995. Isotope studies of granitoids from the
654 Bangenhuk formation, Ny Friesland Caledonides, Svalbard. Geol. Mag. 132, 303-320.
655 Johansson, Å., Gee, D.G., 1999. The late Palaeoproterozoic Eskolabreen granitoids of southern Ny
656 Friesland, Svalbard Caledonides-geochemistry, age, and origin. GFF 121, 113-126.
657 Johansson, Å., Larionov, A.N., Tebenkov, A.M., Gee, D.G., Whitehouse, M.J., Vestin, J., 2000.
658 Grenvillian magmatism of western and central Nordaustlandet, northeastern Svalbard. Earth
659 Env. Sci. T. R. So. 90, 221-254.
660 Johansson, Å., Larionov, A.N., Tebenkov, A.M., Ohta, Y., Gee, D.G., 2002. Caledonian granites of
661 western and central Nordaustlandet, northeast Svalbard. GFF 124, 135-148.
662 Kim, J.-H., Torres, M.E., Haley, B.A., Kastner, M., Pohlman, J.W., Riedel, M., Lee, Y.-J., 2012. The
663 effect of diagenesis and fluid migration on rare earth element distribution in pore fluids of the
664 northern Cascadia accretionary margin. Chem. Geol. 291, 152-165.

665 Konhauser, K.O., Lalonde, S.V., Planavsky, N.J., Pecoits, E., Lyons, T.W., Mojzsis, S.J., Rouxel, O.J.,
666 Barley, M.E., Rosìere, C., Fralick, P.W., 2011. Aerobic bacterial pyrite oxidation and acid rock
667 drainage during the Great Oxidation Event. Nature 478, 369-373.
668 Kraft, S., Frank, M., Hathorne, E.C., Weldeab, S., 2013. Assessment of seawater Nd isotope
669 signatures extracted from foraminiferal shells and authigenic phases of Gulf of Guinea
670 sediments. Geochim. Cosmochim. Acta 121, 414-435.
671 Lacan, F., Jeandel, C., 2004. Neodymium isotopic composition and rare earth element concentrations
672 in the deep and intermediate Nordic Seas: Constraints on the Iceland Scotland Overflow Water
673 signature. Geochem. Geophys. Geosyst. 5, 10.1029/2004GC000742.
674 Lacan, F., Jeandel, C., 2005. Acquisition of the neodymium isotopic composition of the North Atlantic
675 Deep Water. Geochem. Geophys. Geosyst. 6.
676 Langman, J.B., Sinclair, S., Amos, R.T., Wilson, D., Ptacek, C.J., Sego, D.C., Smith, L., Blowes,
677 D.W., 2019. Alkalinity generation from weathering of accessory calcite and apatite and acid
678 drainage neutralization in an Archean granitoid waste rock. J. Geochem. Explor. 205, 106341.
679 Larkin, C.S., Ezat, M.M., Roberts, N.L., Bauch, H.A., Spielhagen, R.F., Noormets, R., Polyak, L.,
680 Moreton, S.G., Rasmussen, T.L., Sarnthein, M., Tipper, E.T., Piotrowski, A.M., 2022. Active
681 Nordic Seas deep-water formation during the last glacial maximum. Nat. Geosci. 15, 925-931.
682 Larkin, C.S., Piotrowski, A.M., Hindshaw, R.S., Bayon, G., Hilton, R.G., Baronas, J.J., Dellinger, M.,
683 Wang, R., Tipper, E.T., 2021. Constraints on the source of reactive phases in sediment from a
684 major Arctic river using neodymium isotopes. Earth Planet. Sci. Lett. 565, 116933.
685 Laufer-Meiser, K., Michaud, A.B., Maisch, M., Byrne, J.M., Kappler, A., Patterson, M.O., Røy, H.,
686 Jørgensen, B.B., 2021. Potentially bioavailable iron produced through benthic cycling in
687 glaciated Arctic fjords of Svalbard. Nat. Commun. 12, 1-13.
688 Laukert, G., Frank, M., Bauch, D., Hathorne, E.C., Rabe, B., von Appen, W.-J., Wegner, C., Zieringer,
689 M., Kassens, H., 2017. Ocean circulation and freshwater pathways in the Arctic Mediterranean
690 based on a combined Nd isotope, REE and oxygen isotope section across Fram Strait.
691 Geochim. Cosmochim. Acta 202, 285-309.

692 Laukert, G., Makhotin, M., Petrova, M.V., Frank, M., Hathorne, E.C., Bauch, D., Böning, P., Kassens,
693 H., 2019. Water mass transformation in the Barents Sea inferred from radiogenic neodymium
694 isotopes, rare earth elements and stable oxygen isotopes. Chem. Geol. 511, 416-430.
695 Lawrence, M.G., Greig, A., Collerson, K.D., Kamber, B.S., 2006. Rare earth element and yttrium
696 variability in south east Queensland waterways. Aquat. Geochem. 12, 39-72.
697 Lee, J., Kim, Y., Cha, J., Kim, D., Jang, K., Kim, J.-H., Nam, S.-I., Hong, S., 2023. Distributions and
698 potential sources of polychlorinated biphenyls and polycyclic aromatic hydrocarbons in the
699 glacimarine sediments of Arctic Svalbard. Mar. Pollut. Bull. 189, 114740.
700 Lemaitre, N., Bayon, G., Ondréas, H., Caprais, J.-C., Freslon, N., Bollinger, C., Rouget, M.-L., de
701 Prunelé, A., Ruffine, L., Olu-Le Roy, K., Sarthou, G., 2014. Trace element behaviour at cold
702 seeps and the potential export of dissolved iron to the ocean. Earth Planet. Sci. Lett. 404, 376-
703 388.
704 León, R., Macías, F., R. Cánovas, C., Pérez-López, R., Ayora, C., Nieto, J.M., Olías, M., 2021. Mine
705 waters as a secondary source of rare earth elements worldwide: The case of the Iberian Pyrite
706 Belt. J. Geochem. Explor. 224, 106742.
707 Lerman, A., Wu, L., 2006. CO2 and sulfuric acid controls of weathering and river water composition.
708 J. Geochem. Explor. 88, 427-430.
709 Liu, W., Xu, Z., Jiang, H., Zhou, X., Zhao, T., Li, Y., 2023. Lithological and glacial controls on sulfide
710 weathering and the associated CO_2 budgets in the Tibetan Plateau: New constraints from small
711 catchments. Geochim. Cosmochim. Acta 343, 341-352.
712 Martin, E.E., Blair, S.W., Kamenov, G.D., Scher, H.D., Bourbon, E., Basak, C., Newkirk, D.N., 2010.
713 Extraction of Nd isotopes from bulk deep sea sediments for paleoceanographic studies on
714 Cenozoic time scales. Chem. Geol. 269, 414-431.
715 McLennan, S.M., 2001. Relationships between the trace element composition of sedimentary rocks
716 and upper continental crust. Geochem. Geophys. Geosyst. 2.
717 Michaud, A.B., Laufer, K., Findlay, A., Pellerin, A., Antler, G., Turchyn, A.V., Røy, H., Wehrmann,
718 L.M., Jørgensen, B.B., 2020. Glacial influence on the iron and sulfur cycles in Arctic fjord

719 sediments (Svalbard). Geochim. Cosmochim. Acta 280, 423-440.
720 Mitra, A., Elderfield, H., Greaves, M.J., 1994. Rare earth elements in submarine hydrothermal fluids
721 and plumes from the Mid-Atlantic Ridge. Mar. Chem. 46, 217-235.
722 Molina-Kescher, M., Frank, M., Hathorne, E., 2014a. South Pacific dissolved Nd isotope
723 compositions and rare earth element distributions: Water mass mixing versus biogeochemical
724 cycling. Geochim. Cosmochim. Acta 127, 171-189.
725 Molina-Kescher, M., Frank, M., Hathorne, E.C., 2014b. Nd and Sr isotope compositions of different
726 phases of surface sediments in the South Pacific: Extraction of seawater signatures, boundary
727 exchange, and detrital/dust provenance. Geochem. Geophys. Geosyst. 15, 3502-3520.
728 Nozaki, Y., Alibo, D.-S., Amakawa, H., Gamo, T., Hasumoto, H., 1999. Dissolved rare earth elements
729 and hydrography in the Sulu Sea. Geochim. Cosmochim. Acta 63, 2171-2181.
730 Nozaki, Y., Alibo, D.S., 2003. Importance of vertical geochemical processes in controlling the oceanic
731 profiles of dissolved rare earth elements in the northeastern Indian Ocean. Earth Planet. Sci.
732 Lett. 205, 155-172.
733 Ohr, M., Halliday, A.N., Peacor, D.R., 1994. Mobility and fractionation of rare earth elements in
734 argillaceous sediments: Implications for dating diagenesis and low-grade metamorphism.
735 Geochim. Cosmochim. Acta 58, 289-312.
736 Osborne, A.H., Haley, B.A., Hathorne, E.C., Plancherel, Y., Frank, M., 2015. Rare earth element
737 distribution in Caribbean seawater: Continental inputs versus lateral transport of distinct REE
738 compositions in subsurface water masses. Mar. Chem. 177, 172-183.
739 Ostrander, C. M., Johnson, A. C., Anbar, A. D., 2021. Earth's first redox revolution. Annu. Rev. Earth
740 Planet. Sci., 49, 337-366.
741 Pérez-López, R., Delgado, J., Nieto, J.M., Márquez-García, B., 2010. Rare earth element
742 geochemistry of sulphide weathering in the São Domingos mine area (Iberian Pyrite Belt): A
743 proxy for fluid–rock interaction and ancient mining pollution. Chem. Geol. 276, 29-40.
744 Pin, C., Zalduegui, J.S., 1997. Sequential separation of light rare-earth elements, thorium and uranium
745 by miniaturized extraction chromatography: Application to isotopic analyses of silicate rocks.

746 Anal. Chim. Acta 339, 79-89.
747 Piotrowski, A.M., Goldstein, S.L., Hemming, S.R., Fairbanks, R.G., 2004. Intensification and
748 variability of ocean thermohaline circulation through the last deglaciation. Earth Planet. Sci.
749 Lett. 225, 205-220.
750 Poulton, S.W., Canfield, D.E., 2005. Development of a sequential extraction procedure for iron:
751 implications for iron partitioning in continentally derived particulates. Chem. Geol. 214, 209-
752 221.
753 Roberts, N.L., Piotrowski, A.M., McManus, J.F., Keigwin, L.D., 2010. Synchronous deglacial
754 overturning and water mass source changes. Science 327, 75-78.
755 Rongemaille, E., Bayon, G., Pierre, C., Bollinger, C., Chu, N.C., Fouquet, Y., Riboulot, V., Voisset,
756 M., 2011. Rare earth elements in cold seep carbonates from the Niger delta. Chem. Geol. 286,
757 196-206.
758 Røthe, T.O., Bakke, J., Vasskog, K., Gjerde, M., D'Andrea, W.J., Bradley, R.S., 2015. Arctic Holocene
759 glacier fluctuations reconstructed from lake sediments at Mitrahalvøya, Spitsbergen. Quat. Sci.
760 Rev. 109, 111-125.
761 Rutberg, R.L., Hemming, S.R., Goldstein, S.L., 2000. Reduced North Atlantic Deep Water flux to the
762 glacial Southern Ocean inferred from neodymium isotope ratios. Nature 405, 935-938.
763 Schijf, J., De Baar, H.J.W., Millero, F.J., 1995. Vertical distributions and speciation of dissolved rare
764 earth elements in the anoxic brines of Bannock Basin, eastern Mediterranean Sea. Geochim.
765 Cosmochim. Acta 59, 3285-3299.
766 Shiller, A.M., Chan, E.W., Joung, D.J., Redmond, M.C., Kessler, J.D., 2017. Light rare earth element
767 depletion during Deepwater Horizon blowout methanotrophy. Sci. Rep. 7, 10389.
768 Sholkovitz, E.R., Piepgras, D.J., Jacobsen, S.B., 1989. The pore water chemistry of rare earth
769 elements in Buzzards Bay sediments. Geochim. Cosmochim. Acta 53, 2847-2856.
770 Sholkovitz, E.R., Shaw, T.J., Schneider, D.L., 1992. The geochemistry of rare earth elements in the
771 seasonally anoxic water column and porewaters of Chesapeake Bay. Geochim. Cosmochim.
772 Acta 56, 3389-3402.

773 Skinner, L.C., Sadekov, A., Brandon, M., Greaves, M., Plancherel, Y., de la Fuente, M., Gottschalk, J.,
774 Souanef-Ureta, S., Sevilgen, D.S., Scrivner, A.E., 2019. Rare earth elements in early-
775 diagenetic foraminifer 'coatings': Pore-water controls and potential palaeoceanographic
776 applications. Geochim. Cosmochim. Acta 245, 118-132.
777 Soyol-Erdene, T.-O., Huh, Y., 2013. Rare earth element cycling in the pore waters of the Bering Sea
778 Slope (IODP Exp. 323). Chem. Geol. 358, 75-89.
779 Stachnik, Ł., Yde, J.C., Krzemień, K., Uzarowicz, Ł., Sitek, S., Kenis, P., 2022. SEM-EDS and water
780 chemistry characteristics at the early stages of glacier recession reveal biogeochemical
781 coupling between proglacial sediments and meltwater. Sci. Total Environ. 835, 155383.
782 Stichel, T., Frank, M., Rickli, J., Hathorne, E.C., Haley, B.A., Jeandel, C., Pradoux, C., 2012. Sources
783 and input mechanisms of hafnium and neodymium in surface waters of the Atlantic sector of
784 the Southern Ocean. Geochim. Cosmochim. Acta 94, 22-37.
785 Süfke, F., Gutjahr, M., Gilli, A., Anselmetti, F.S., Glur, L., Eisenhauer, A., 2019. Early stage
786 weathering systematics of Pb and Nd isotopes derived from a high-Alpine Holocene lake
787 sediment record. Chem. Geol. 507, 42-53.
788 Svendsen, J.I., Mangerud, J., 1997. Holocene glacial and climatic variations on Spitsbergen, Svalbard.
789 The Holocene 7, 45-57.
790 Tachikawa, K., Jeandel, C., Roy-Barman, M., 1999. A new approach to the Nd residence time in the
791 ocean: the role of atmospheric inputs. Earth Planet. Sci. Lett. 170, 433-446.
792 Tachikawa, K., Piotrowski, A.M., Bayon, G., 2014. Neodymium associated with foraminiferal
793 carbonate as a recorder of seawater isotopic signatures. Quat. Sci. Rev. 88, 1-13.
794 Takaya, Y., Fujinaga, K., Yamagata, N., Araki, S., Maki, R., Nakamura, K., Iijima, K., Kato, Y., 2015.
795 Chemical leaching of rare earth elements from highly REY-rich mud. Geochem. J. 49, 637-
796 652.
797 Taylor, S.R., McLennan, S.M., 1985. The continental crust: its composition and evolution.
798 Tazoe, H., Obata, H., Gamo, T., 2011. Coupled isotopic systematics of surface cerium and neodymium
799 in the Pacific Ocean. Geochem. Geophys. Geosyst. 12.

800 Torres, M.A., Moosdorf, N., Hartmann, J., Adkins, J.F., West, A.J., 2017. Glacial weathering, sulfide
801 oxidation, and global carbon cycle feedbacks. Proc. Natl. Acad. Sci. 114, 8716-8721.
802 Turchyn, A.V., Schrag, D.P., 2004. Oxygen Isotope Constraints on the Sulfur Cycle over the Past 10
803 Million Years. Science 303, 2004-2007.
804 Vance, D., Teagle, D.A., Foster, G.L., 2009. Variable Quaternary chemical weathering fluxes and
805 imbalances in marine geochemical budgets. Nature 458, 493-496.
806 Vogt, C., Jang, K., 2023. Bulk mineral assemblage of sediment cores from Svalbard fjords determined
807 via full pattern QXRD. PANGAEA, p. doi:10.1594/PANGAEA.955819.
808 Wadham, J.L., Hawkings, J.R., Tarasov, L., Gregoire, L.J., Spencer, R.G.M., Gutjahr, M., Ridgwell,
809 A., Kohfeld, K.E., 2019. Ice sheets matter for the global carbon cycle. Nat. Commun. 10,
810 3567.
811 Wang, Z.-L., Yamada, M., 2007. Geochemistry of dissolved rare earth elements in the Equatorial
812 Pacific Ocean. Environ. Geol. 52, 779-787.
813 Wehrmann, L.M., Formolo, M.J., Owens, J.D., Raiswell, R., Ferdelman, T.G., Riedinger, N., Lyons,
814 T.W., 2014. Iron and manganese speciation and cycling in glacially influenced high-latitude
815 fjord sediments (West Spitsbergen, Svalbard): Evidence for a benthic recycling-transport
816 mechanism. Geochim. Cosmochim. Acta 141, 628-655.
817 Wehrmann, L.M., Riedinger, N., Brunner, B., Kamyshny, A., Hubert, C.R.J., Herbert, L.C., Brüchert,
818 V., Jørgensen, B.B., Ferdelman, T.G., Formolo, M.J., 2017. Iron-controlled oxidative sulfur
819 cycling recorded in the distribution and isotopic composition of sulfur species in glacially
820 influenced fjord sediments of west Svalbard. Chem. Geol. 466, 678-695.
821 Werner, K., Frank, M., Teschner, C., Müller, J., Spielhagen, R.F., 2014. Neoglacial change in deep
822 water exchange and increase of sea-ice transport through eastern Fram Strait: evidence from
823 radiogenic isotopes. Quat. Sci. Rev. 92, 190-207.
824 Wilson, D.J., Piotrowski, A.M., Galy, A., Clegg, J.A., 2013. Reactivity of neodymium carriers in deep
825 sea sediments: Implications for boundary exchange and paleoceanography. Geochim.
826 Cosmochim. Acta 109, 197-221.

827 Yang, J., Haley, B., 2016. The profile of the rare earth elements in the Canada Basin, Arctic Ocean.
828 Geochem. Geophys. Geosyst. 17, 3241-3253.
829 Yang, J., Kim, J.-H., Torres, M., Haley, B., 2018. Data report: dissolved rare earth elements (REEs) in
830 the pore fluids of Sites U1378, U1380, U1381, and U1414 drilled during IODP Expeditions
831 334 and 344, Proc. IODP Vol. 344, p. doi:10.2204/iodp.proc.2344.2209.2018.
832 Yeghicheyan, D., Aubert, D., Bouhnik-Le Coz, M., Chmeleff, J., Delpoux, S., Djouraev, I., Granier,
833 G., Lacan, F., Piro, J.-L., Rousseau, T., Cloquet, C., Marquet, A., Menniti, C., Pradoux, C.,
834 Freydier, R., Vieira da Silva-Filho, E., Suchorski, K., 2019. A new interlaboratory
835 characterisation of silicon, rare earth elements and twenty-two other trace element
836 concentrations in the natural river water certified reference material SLRS-6 (NRC-CNRC).
837 Geostand. Geoanal. Res. 43, 475-496.
838 Zhang, J., Nozaki, Y., 1998. Behavior of rare earth elements in seawater at the ocean margin: a study
839 along the slopes of the Sagami and Nankai troughs near Japan. Geochim. Cosmochim. Acta
840 62, 1307-1317.
841 Zhang, R., John, S.G., Zhang, J., Ren, J., Wu, Y., Zhu, Z., Liu, S., Zhu, X., Marsay, C.M., Wenger, F.,
842 2015. Transport and reaction of iron and iron stable isotopes in glacial meltwaters on Svalbard
843 near Kongsfjorden: From rivers to estuary to ocean. Earth Planet. Sci. Lett. 424, 201-211.
844 Zhang, Y., Lacan, F., Jeandel, C., 2008. Dissolved rare earth elements tracing lithogenic inputs over
845 the Kerguelen Plateau (Southern Ocean). Deep-Sea Res. II 55, 638-652.
846 Zhao, Y., Wei, W., Santosh, M., Hu, J., Wei, H., Yang, J., Liu, S., Zhang, G., Yang, D., Li, S., 2022. A
847 review of retrieving pristine rare earth element signatures from carbonates. Palaeogeogr.
848 Palaeoclimatol. Palaeoecol. 586, 110765.
849 Zheng, X.-Y., Plancherel, Y., Saito, M.A., Scott, P.M., Henderson, G.M., 2016. Rare earth elements
850 (REEs) in the tropical South Atlantic and quantitative deconvolution of their non-conservative
851 behavior. Geochim. Cosmochim. Acta 177, 217-237.

852

Figure 1

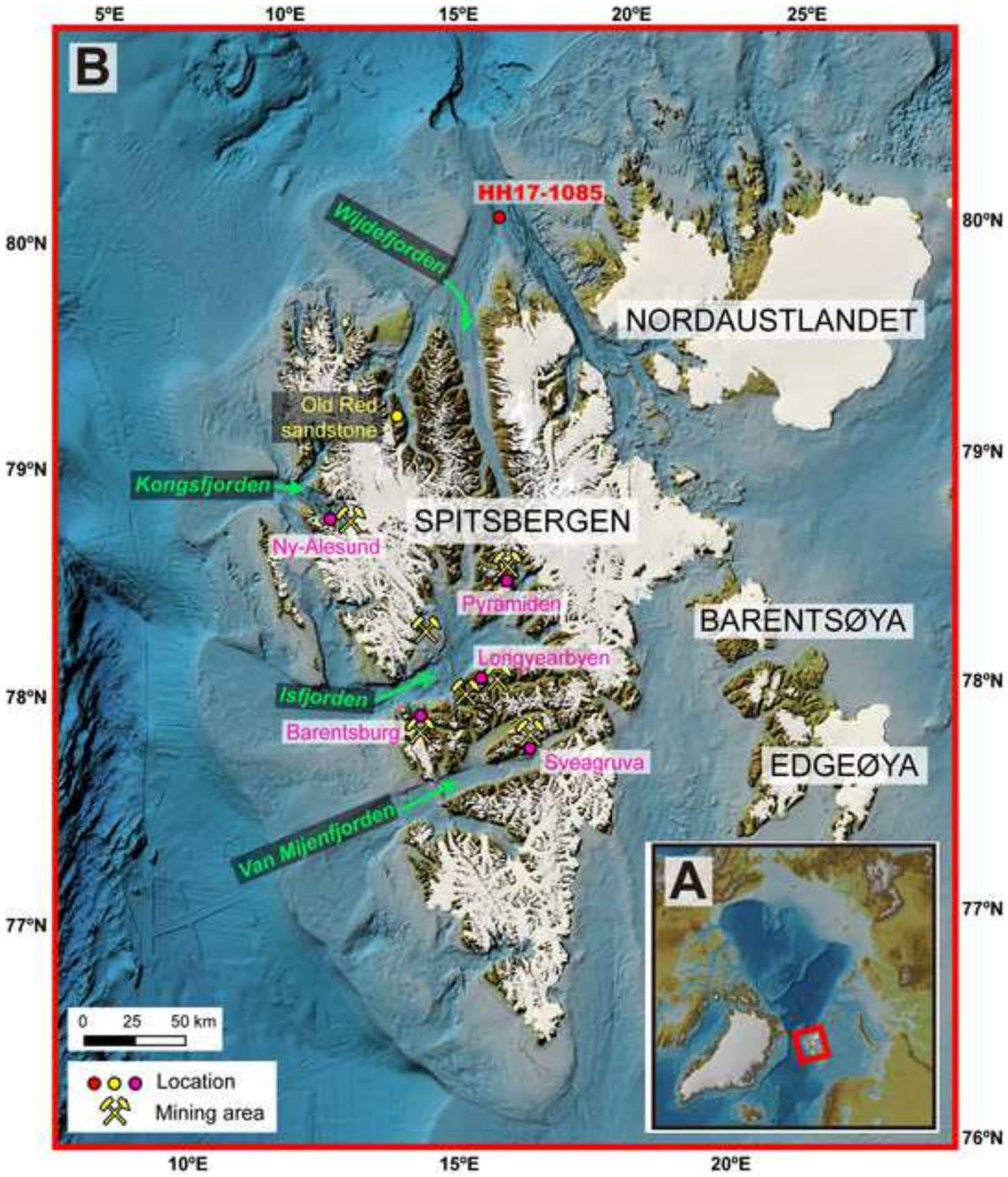
B
5°E
10°E
15°E
20°E
25°E
80°N
79°N
78°N
77°N
76°N
HH17-1085
Wijdefjorden
NORDAUSTLANDET
Old Red sandstone
Kongsfjorden
SPITSBERGEN
Ny-Ålesund
Pyramiden
BARENTSØYA
Longyearbyen
Isfjorden
Barentsburg
Sveagruva
EDGEØYA
Van Mijenfjorden
A
0 25 50 km
Location
Mining area

Figure 2.

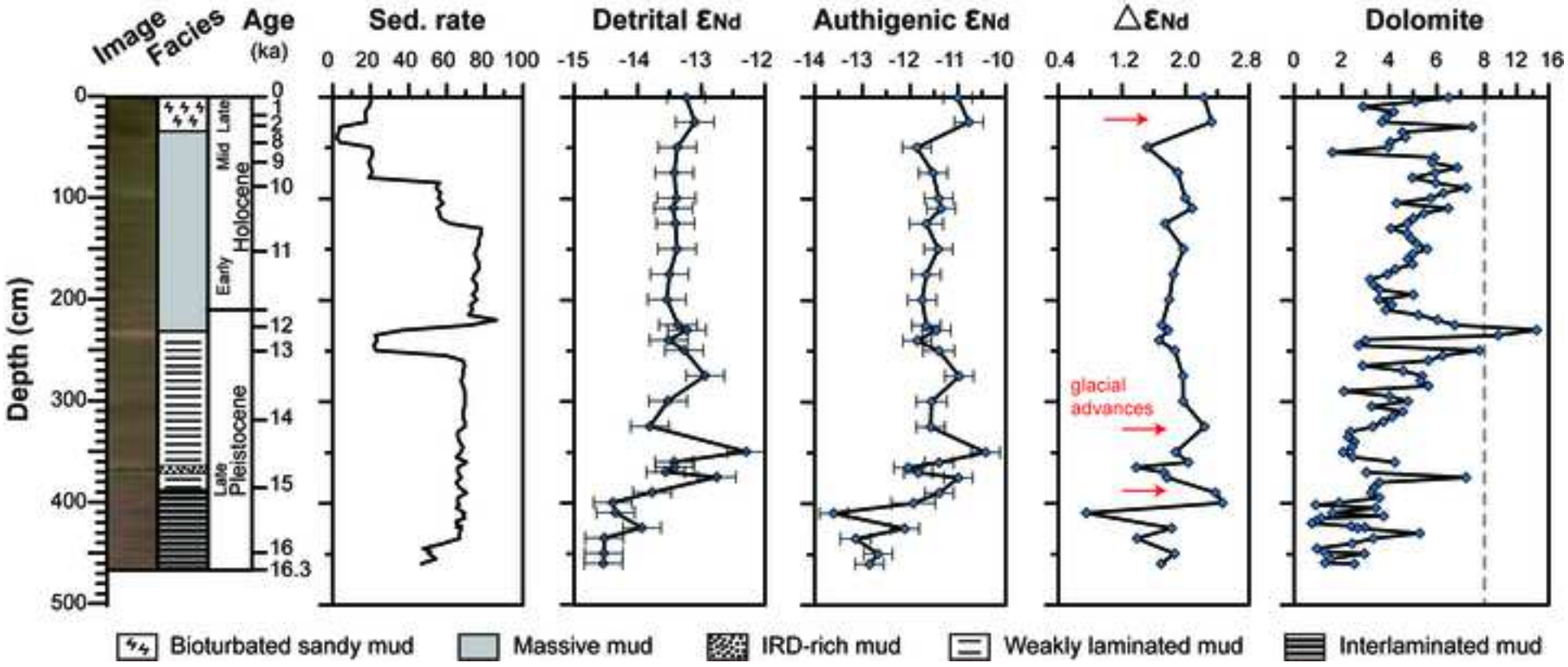
Image
Facies
Age
(ka)
Sed. rate
Detrital εNd
Authigenic εNd
△εNd
Dolomite
Depth (cm)
Mid Late
Holocene
Early
Late
Pleistocene
glacial
advances
Bioturbated sandy mud
Massive mud
IRD-rich mud
Weakly laminated mud
Interlaminated mud

Figure 3.

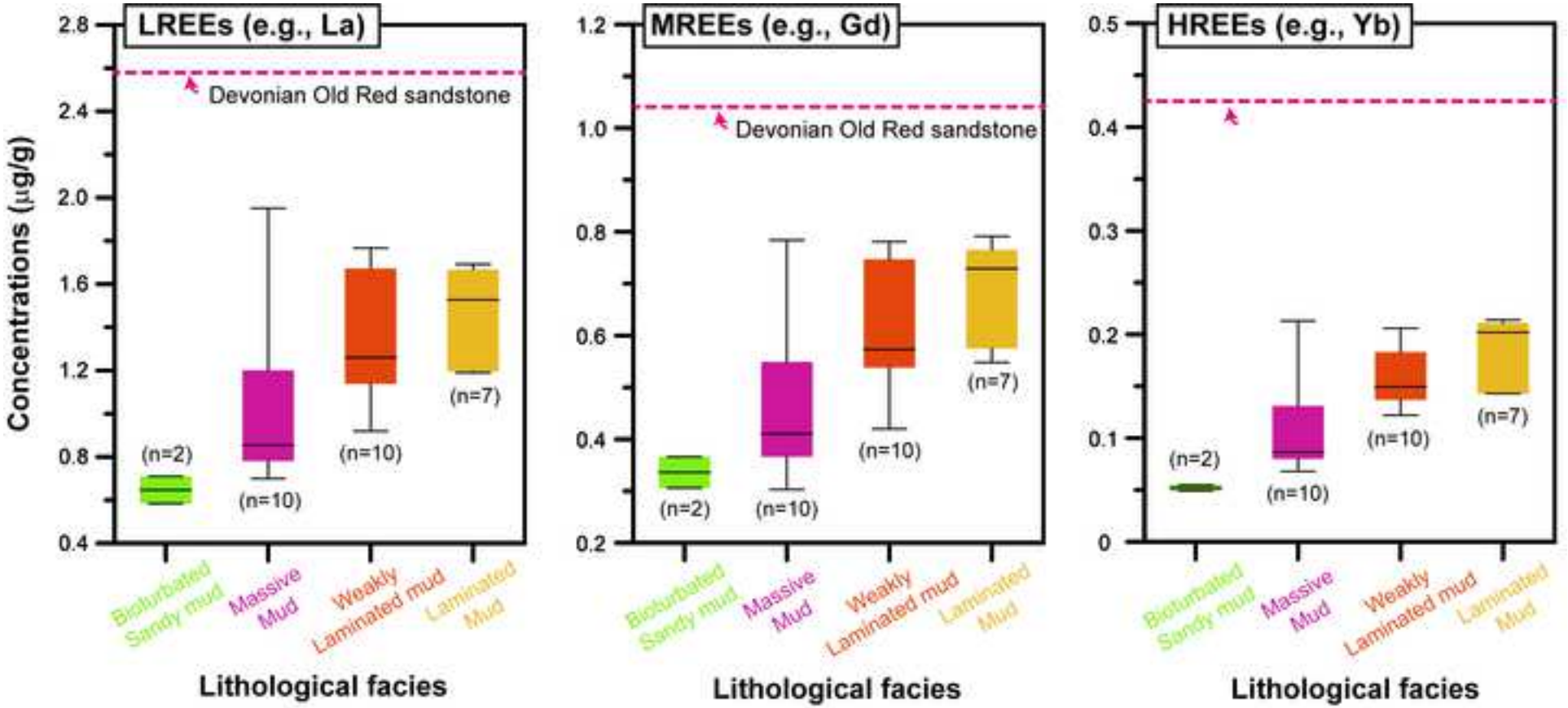
LREEs (e.g., La)
Devonian Old Red sandstone
Concentrations (μg/g)
2.8
2.4
2.0
1.6
1.2
0.8
0.4
(n=2)
(n=10)
(n=10)
(n=7)
Bioturbated Sandy mud
Massive Mud
Weakly Laminated mud
Laminated Mud
Lithological facies
MREEs (e.g., Gd)
Devonian Old Red sandstone
1.2
1.0
0.8
0.6
0.4
0.2
(n=2)
(n=10)
(n=10)
(n=7)
Bioturbated Sandy mud
Massive Mud
Weakly Laminated mud
Laminated Mud
Lithological facies
HREEs (e.g., Yb)
0.5
0.4
0.3
0.2
0.1
0
(n=2)
(n=10)
(n=10)
(n=7)
Bioturbated Sandy mud
Massive Mud
Weakly Laminated mud
Laminated Mud
Lithological facies

Figure 4

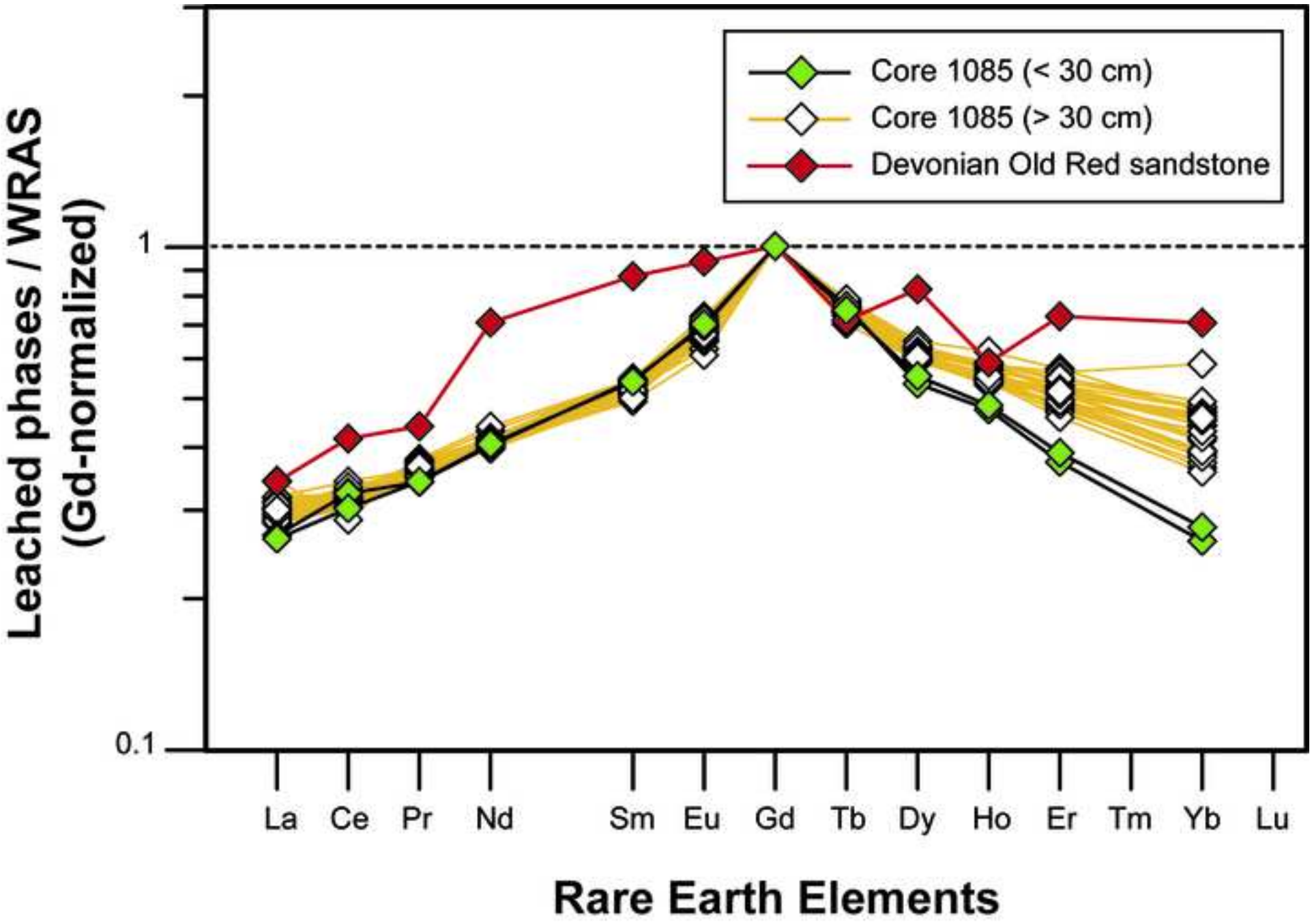
Core 1085 (< 30 cm)
Core 1085 (> 30 cm)
Devonian Old Red sandstone
Leached phases / WRAS
(Gd-normalized)
1
0.1
La
Ce
Pr
Nd
Sm
Eu
Gd
Tb
Dy
Ho
Er
Tm
Yb
Lu
Rare Earth Elements

Figure 5

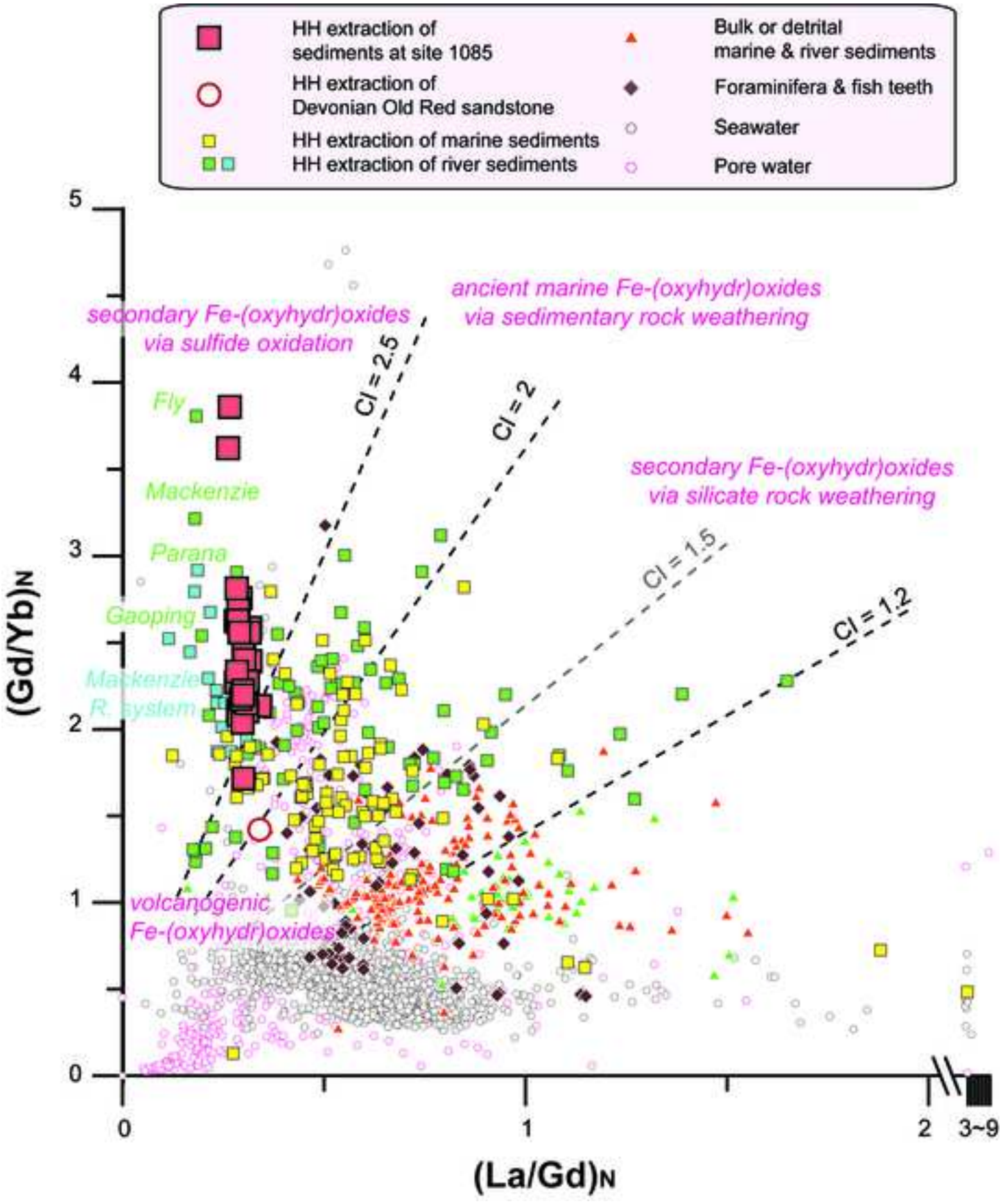
HH extraction of sediments at site 1085
HH extraction of Devonian Old Red sandstone
HH extraction of marine sediments
HH extraction of river sediments
Bulk or detrital marine & river sediments
Foraminifera & fish teeth
Seawater
Pore water
ancient marine Fe-(oxyhydr)oxides via sedimentary rock weathering
secondary Fe-(oxyhydr)oxides via sulfide oxidation
secondary Fe-(oxyhydr)oxides via silicate rock weathering
volcanogenic Fe-(oxyhydr)oxides
Cl = 2.5
Cl = 2
Cl = 1.5
Cl = 1.2
Fly
Mackenzie
Parana
Gaoping
Mackenzie R. system
(Gd/Yb)N
(La/Gd)N
0
1
2
3
4
5
0
1
2
3~9

Figure 6

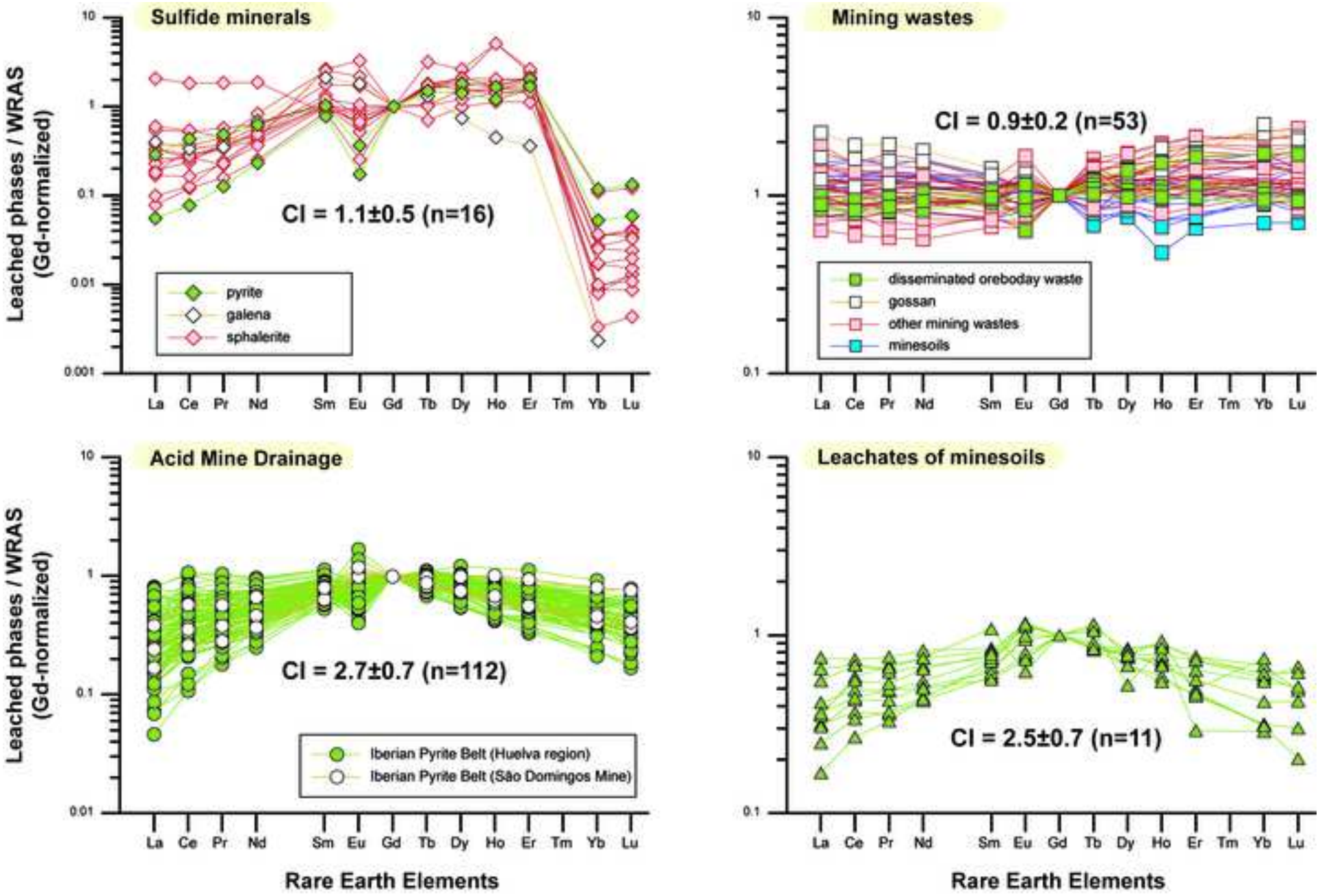
Sulfide minerals
Cl = 1.1±0.5 (n=16)
pyrite
galena
sphalerite
Mining wastes
Cl = 0.9±0.2 (n=53)
disseminated oreboday waste
gossan
other mining wastes
minesoils
Acid Mine Drainage
Cl = 2.7±0.7 (n=112)
Iberian Pyrite Belt (Huelva region)
Iberian Pyrite Belt (São Domingos Mine)
Leachates of minesoils
Cl = 2.5±0.7 (n=11)
Leached phases / WRAS (Gd-normalized)
Rare Earth Elements
La Ce Pr Nd Sm Eu Gd Tb Dy Ho Er Tm Yb Lu

Figure 7

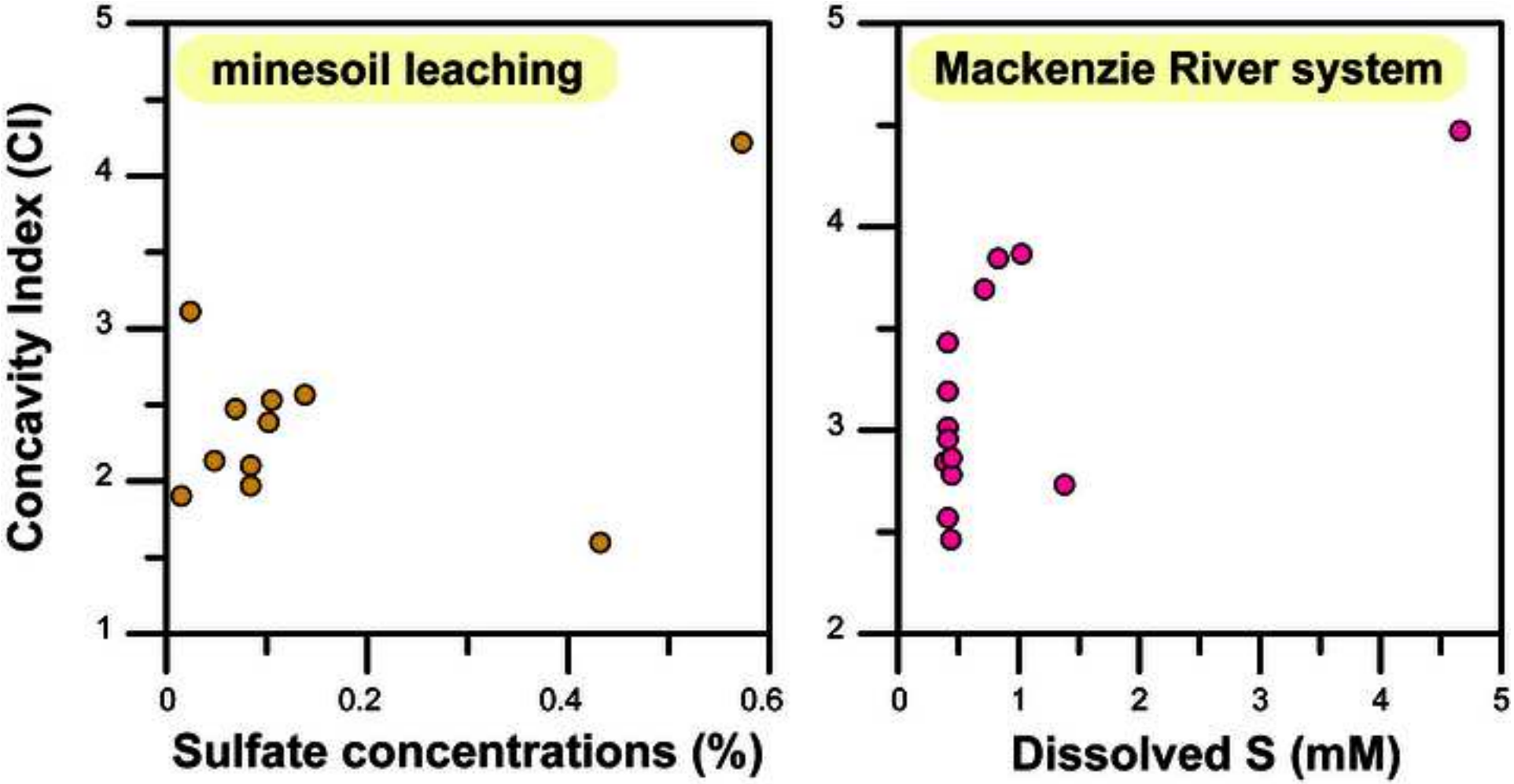
minesoil leaching
Concavity Index (CI)
Sulfate concentrations (%)
0
0.2
0.4
0.6
1
2
3
4
5
Mackenzie River system
Dissolved S (mM)
0
1
2
3
4
5
2

Figure 8

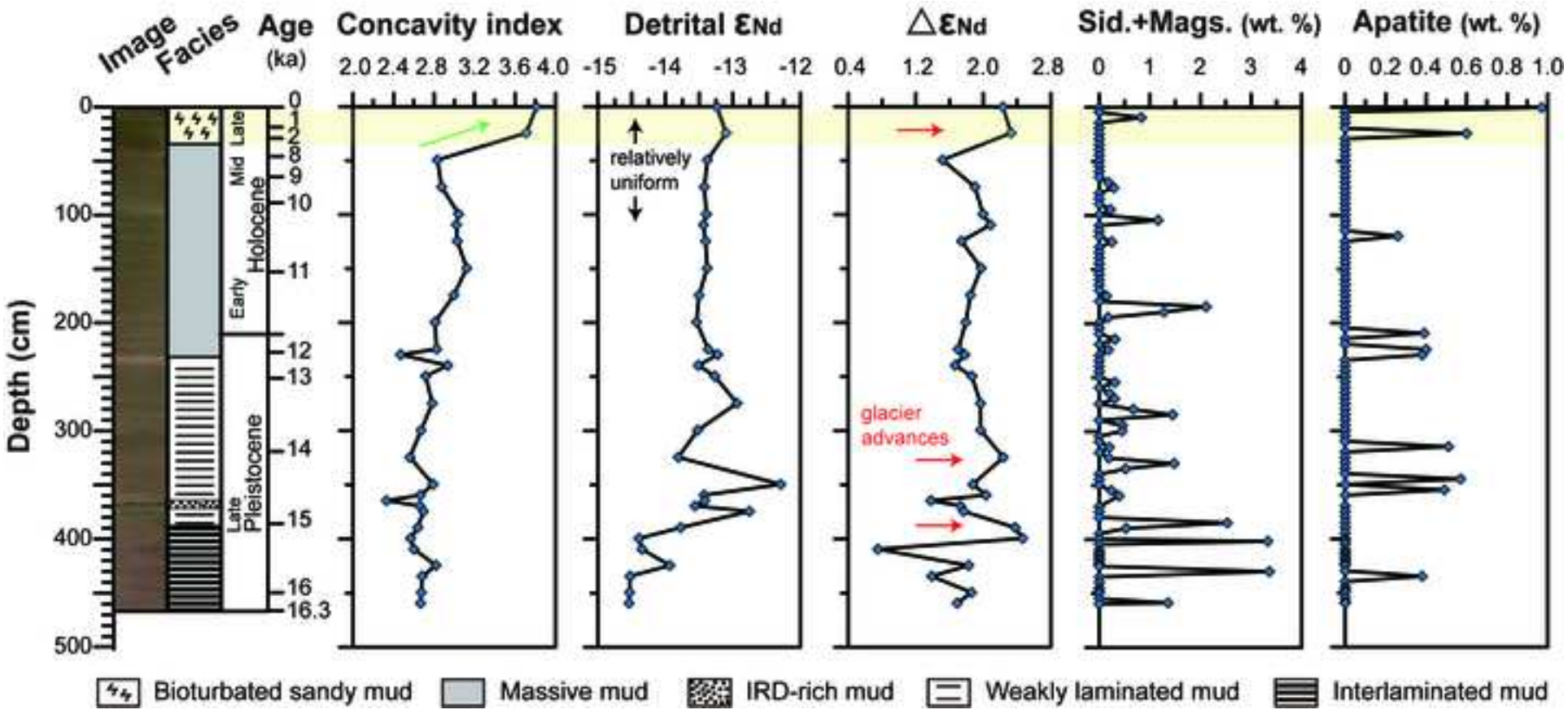
Image
Facies
Age
(ka)
Concavity index
Detrital εNd
△εNd
Sid.+Mags. (wt. %)
Apatite (wt. %)
Depth (cm)
Late
Mid
Early
Holocene
Late
Pleistocene
relatively
uniform
glacier
advances
Bioturbated sandy mud
Massive mud
IRD-rich mud
Weakly laminated mud
Interlaminated mud